The Astrophysical Journal, 588:264–280, 2003 May 1

DIFFUSE X-RAY EMISSION FROM M101

K. D. Kuntz[1]
Department of Physics, University of Maryland Baltimore County, 1000 Hilltop Circle, Baltimore MD 21250

and

S. L. Snowden,[2] W. D. Pence, and K. Mukai[2]
Laboratory for High Energy Astrophysics, Code 662, NASA Goddard Space Flight Center, Greenbelt, MD 20771;
snowden@riva.gsfc.nasa.gov, pence@tetra.gsfc.nasa.gov, mukai@milkyway.gsfc.nasa.gov
Received 2002 October 16; accepted 2003 January 10

ABSTRACT

The total 0.45–1.0 keV luminosity of M101 is 3.2×10^{39} ergs s^{-1}, of which 2.3×10^{39} ergs s^{-1} is due to diffuse emission. (*Chandra* observes only ~60% of the diffuse emission observed by *ROSAT* because of its superior point-source detection.) Of the diffuse emission seen by *Chandra*, no more than 6% can be due to luminous unresolved point sources, such as X-ray binaries, and ~10% is likely due to dwarf stars. The diffuse emission traces the spiral arms and is roughly correlated with the Hα and far-UV emission. The radial distribution closely follows the optical profile. The bulk of the diffuse emission is characterized by a two–thermal component spectrum with $kT = 0.20$ and 0.75 keV, and the ratio of the emission measures of the two components is roughly constant as a function of both radius and surface brightness. The softer component has a sufficiently large covering factor that the bulk of the emission is likely extraplanar. We find no evidence of an extended axisymmetric X-ray halo, suggesting that any such halo has a strength much smaller than current predictions.

Subject headings: galaxies: halos — galaxies: individual (M101, NGC 5457) — galaxies: ISM — X-rays: diffuse background — X-rays: galaxies — X-rays: ISM

1. INTRODUCTION

M101 (NGC 5457) is a nearby face-on spiral galaxy that lies in a direction of low Galactic absorption. As such, it is an ideal target for the study of the hot component of the interstellar medium (ISM) in a "typical" spiral galaxy, allowing high spatial resolution and more complete point-source detection at relatively soft energies. Although M101 has a somewhat later Hubble type and is somewhat larger and somewhat less massive than the Milky Way (Table 1), the study of the hot ISM in M101 can aid the study of the hot ISM in the Milky Way since it allows a complete census of the hot gas and a rough indication of its spatial distribution. Absorption by the ISM of the Milky Way produces great uncertainty in our understanding of both the amount of hot gas and its distribution within the Galaxy. Although such a study of M101 cannot directly measure the filling factor of hot gas or determine its immediate sources (because of source confusion), it will provide some general constraints on the evolutionary history of hot gas, its movement through the disk-halo interface, and the extent to which it may fill the dark matter potential.

1.1. *Previous Results*

Previous studies of the diffuse emission from M101 have been executed with *Einstein* (McCammon & Sanders 1984; Trinchieri, Fabbiano, & Romaine 1990), the *Röntgen-Satellit* (*ROSAT*) Position Sensitive Proportional Counter (PSPC; Snowden & Pietsch 1995; Wang, Immler, & Pietsch 1999), the *ROSAT* High Resolution Imager (HRI; Wang et al. 1999), and the *Advanced Satellite for Cosmology and Astrophysics* (*ASCA*; Wang et al. 1999). These studies are characterized by relatively poor spatial resolution that hindered point-source detection and placed large uncertainties on the amount of diffuse emission.

The PSPC study demonstrated the existence of diffuse $\frac{1}{4}$ keV emission with a filling factor of ~1 and a color temperature of $10^{5.8}$ K ($kT = 0.054$ keV) The temperature and large filling factor prompted the authors to suggest that the $\frac{1}{4}$ keV emission was primarily in the halo; if the emission were from the disk and due to regions like the Local Hot Bubble (LHB; Snowden et al. 1998), with a typical overburden of a few times 10^{20} cm^{-2}, then the filling fraction would be significantly more than unity and the temperature would be much smaller than that observed for hot Galactic bubbles. Given a resolution of ~1′, a primary concern was the contribution to the diffuse emission by unresolved point sources. Arguments were made that there was no known population of sources that could produce the amount of $\frac{1}{4}$ keV emission seen.

A PSPC study of the $\frac{3}{4}$ keV band (R45, 0.44–1.21 keV) is more comparable to the present *Chandra* study. Snowden & Pietsch (1995) determined an R45 band color temperature of $kT = 0.29$ keV ($T = 10^{6.53}$ K), a flux of 5.8×10^{-13} ergs cm^{-2} s^{-1} within the inner 7.′5, and a luminosity of 3.6×10^{39} ergs s^{-1}. Again there was a concern about the contributions from unresolved point sources, but there were insufficient source statistics to attempt a correction. Contributions from sources such as M dwarfs could be reasonably well constrained and shown to be small.

Wang et al. (1999) also came to the conclusion that no known population of sources could explain the entire emission seen in the central region of M101. They further attempted to constrain the temperature of the diffuse emission in the central 5′ with a joint fit to the *ROSAT* PSPC

[1] Mailing address: Laboratory for High Energy Astrophysics, Code 662, NASA Goddard Space Flight Center, Greenbelt, MD 20771; kuntz@milkyway.gsfc.nasa.gov.
[2] Universities Space Research Association.

TABLE 1
M101 (NGC 5457) PARTICULARS

PARAMETER	M101		MILKY WAY	
	Value	Source	Value	Source
Distance (Mpc)	7.2 (2.09 kpc arcmin^{-1})	Stetson et al. 1998	...	...
Position (J2000.0)	$\alpha = 14\,03\,12.7$, $\delta = 54\,20\,56$	...	...	...
Inclination (deg)	27 ± 1	Kamphuis 1993	...	...
Line of nodes (deg)	35 ± 1	Zaritsky, Elston, & Hill 1990[a]	...	...
$N_{\rm H}$(foreground) (cm^{-2})	$8.8^{-1} \times 10^{19}$ cm^{-2}	Hartmann & Burton 1997	...	...
Hubble type	Scd	Tully 1988	Sb–Sbc	Kerr 1993
H I mass ($M_\odot$)	2.1×10^{10}	Kamphuis 1993	$(3.5–7.0) \times 10^9$	Dame 1993
Mass ($M_\odot$)	2.1×10^{11}	Kamphuis 1993	$(7 \pm 2.5) \times 10^{11}$	Binney & Merrifield 1998
	1.0×10^{11}	Comte, Monnet, & Rosado 1979	$2.4^{+1.3}_{-0.7} \times 10^{11}$	Little & Tremaine 1987
D_{25}	23.′8 (49.8 kpc)	Tully 1988	24.63 kpc	Binney & Merrifield 1998
	...	...	26.71 kpc	van der Kruit 1990
v_c (km s^{-1})	~170	Kamphuis 1993	~220	...
$L_{\rm FIR}$ (ergs s^{-1})	$(3.4 \pm 0.3) \times 10^{43}$[b]	Beck & Golla 1988	3.0×10^{43}	Sodroski et al. 1997
SN rate (century^{-1})	2	Matonick & Fesen 1997	...	...

NOTE.—Units of right ascension are hours, minutes, and seconds, and units of declination are degrees, arcminutes, and arcseconds.
[a] The Zaritsky et al. 1990 values are representative of a number of measures made in the 1970s and 1980s, although the spread of values is somewhat larger than the uncertainties would indicate.
[b] Value summed over the entire disk. Note that the value in Fullmer & Lonsdale 1989 is for a point source at the location of M101.

and *ASCA* Gas Imaging Spectrometer (GIS) spectra. Given the angular resolution of the PSPC and the poorer angular resolution of the GIS, they did not attempt to remove the point sources, but they attempted to compensate by modeling the aggregate spectrum of the point sources. Modeling the point sources with either thermal or power-law spectra produced a diffuse component with $kT = 0.186$ keV ($T = 10^{6.335}$ K).

1.2. *Aim of the Present Work*

The angular resolution of *Chandra* not only allows point-source detection and removal to unprecedented levels, but it also allows the construction of the point-source luminosity function, the extrapolation of which places upper limits on the possible contribution of unresolved sources to the diffuse emission. The catalog of point sources and the luminosity function was presented in Pence et al. (2001), while discussion of some individual objects is contained in Snowden et al. (2001) and Mukai et al. (2003). The purpose of the present work is to determine the distribution, luminosity, and gross spectral characteristics of the soft diffuse X-ray emission from M101.

The electronic noise feature effectively limits the *Chandra* energy interval to $E > 0.45$ keV, while the response is negligible for $E \gtrsim 10$ keV. In this energy interval the disk of M101 ranges from nearly transparent at high energies to, at worst, $\tau \sim 2.7$ at 0.45 keV. Since M101 is nearly face-on, we are "X-raying" the entire disk, detecting most of the gas hot enough to produce significant emission above 0.5 keV. The observed emission will contain contributions from H II regions, supernova remnants (SNRs), hot bubbles, and galactic chimneys, but the faintness of each individual object, or the lack of contrast from neighboring emission regions, restricts the spectral analysis to the bulk properties of the hot gas.

In the following, § 2 describes the gross properties of the data, their reduction, calibration, and point-source removal. Section 3 describes the large-scale diffuse emission, its morphology, hardness ratio, and spectroscopy. Section 4 describes the diffuse emission due to the nuclear/bulge region as well as that due to the giant H II regions NGC 5462 and NGC 5461. Section 5 discusses the extent to which M101 may be viewed as a Milky Way analog and attempts to identify the observed spectroscopic components with similar structures observed in the Milky Way and Magellanic Clouds.

2. DATA

The data analyzed here are derived from a single 98.2 ks *Chandra* exposure taken in AO1 using the Advanced CCD Imaging Spectrometer (ACIS) S3 back-side–illuminated chip. The aim point was placed near the nucleus and the roll angle adjusted so that the bulk of the $\frac{1}{4}$ keV emission detected by *ROSAT*, as well as the giant H II regions NGC 5461 and NGC 5462, would fall on the S3 chip. The configuration was also chosen to maximize the radial extent over which we could study the emission, while leaving space for "blank" sky from which to determine the background. Other chips were on during the exposure but, because of their distance from the aim point or poorer low-energy response, are of little use for this analysis. The most recent gain files were used; response and redistribution functions were extracted from the *Chandra* Interactive Analysis of Observations (CIAO) Calibration Database, version 2.12.

The light curve was constructed for the entire chip in the 2.0–7.0 keV band to allow the detection and removal of background flares. Three minor flares were detected and discarded, reducing the exposure to 92.3 ks. There are often low-level flares that are undetectable from the light curve but that produce a significant spectral signature in the 2.0–7.0 keV band. The contribution from these flares is discussed in § 3.1.1.

2.1. *Point-Source Removal*

Although the bulk of the diffuse emission lies below ~1.5 keV, in order to produce the cleanest spectrum of the diffuse emission we removed sources detected to 3.5 σ in any

of a series of energy bands covering the entire *Chandra* energy range. Point sources were detected using the "wavdetect" routine in the 0.35–1.3, 0.5–2.0, and 2.0–8.0 keV bands. (All of the subbands used in Pence et al. 2001 were processed in a similar way, but did not produce significant sources that had not been found in the three bands listed here.) Significance was determined using Poisson statistics; the source counts were determined from an elliptical 75% encircled energy region with the same aspect ratio and orientation as the point-spread function (PSF) at the source position, and the background counts were determined from a concentric elliptical annulus extending from 2 to 3 times the 95% encircled energy radius. A larger region was removed from around source P98 (Pence et al. 2001) because of its extreme brightness.

The $\log N - \log S$ relation in the 0.5–2.0 keV energy interval is shown in Pence et al. (2001) and extends to luminosities $\sim 10^{36}$ ergs s^{-1}. Extrapolating the $\log N - \log S$ to lower luminosities is not trivial because of rapid changes in the source population with luminosity. In the Galaxy, the low-mass X-ray binary (LMXB) population dominates for 10^{36} ergs s$^{-1} < L < 10^{38}$ ergs s^{-1}, but tails off sharply below 10^{36} ergs s^{-1}. High-mass X-ray binaries (HMXBs) with evolved companions have luminosities 10^{35} ergs s$^{-1} < L < 10^{37}$ ergs s^{-1}, but only half the spatial density of persistent LMXBs (Grimm, Gilfanov, & Sunyaev 2002). Below 10^{35} ergs s^{-1}, a number of other populations exist (such as persistent Be X-ray binaries) whose density with respect to that of LMXBs is poorly understood. Assuming a source spectrum with $\Gamma = 2$ and directly extrapolating the Pence et al. (2001) $\log N - \log S$ relation to luminosities 10^{35} and 10^{34} ergs s^{-1} produces 4.1% and 5.8% of the observed diffuse emission, respectively.

3. LARGE-SCALE DIFFUSE EMISSION

3.1. *Morphology and Photometry*

Figure 1 displays the chip S3 data after point-source removal and smoothing by a 7.″9 FWHM Gaussian. The lower parts of Figure 1 contain the optical and H I 21 cm images. It is immediately apparent that the X-ray emission is strongly correlated with the spiral arms and that a significant fraction of the X-ray emission is due to the giant H II regions NGC 5461 and NGC 5462. The nuclear emission is, in fact, smaller than the emission in either of the giant H II regions. Many, but not all, of the knots of X-ray emission are correlated with H II regions (see Fig. 2), and the stronger knots have associated "point sources" that may be, alternatively, compact diffuse emission regions or compact clusters of X-ray sources. The correlation of X-ray emission with the H I holes is as poor as the correlation between H I holes and Hα emission noted by Kamphuis (1993). Since the lifetime over which an H I hole can be observed is $\sim 5 \times 10^7$ yr and the generating H II regions last $\sim 2 \times 10^7$ yr, Kamphuis argued that two-fifths of the holes should contain H II regions. In our sample, there are 13 large H I holes; three are clearly filled with emission stronger than that of the surrounding disk, another three have X-ray emission comparable to the surrounding disk, and seven have less X-ray emission than the surrounding disk. The H I holes that are filled by X-ray emission tend to have H II regions that are not near the peak of the X-ray emission, while X-ray–empty H I holes tend to have X-ray emission and correlated H II regions on their edges.

We have compared the *Chandra* image with a far-ultraviolet (FUV; 1521 Å) image from the Ultraviolet Imaging Telescope (UIT; Stecher et al. 1997). As can be seen in Figure 2, the regions of diffuse X-ray emission are, in general, well correlated with the regions of diffuse FUV emission. Most knots of X-ray emission are correlated with knots of FUV emission. However, there are some notable exceptions, particularly the diffuse emission around P98 (which may, in fact, be due to the wings of the PSF) and the arclike emission region northeast of the nucleus. A number of the more intense FUV emission knots are not associated with peaks in the X-ray emission. Some of these knots of FUV emission are on the *edges* of knots of X-ray emission, perhaps suggesting the propagation of star formation. The knot of X-ray emission may be associated with SNRs or an aggregation of young X-ray binaries, while the adjacent FUV emission region may be associated with young high-mass stars.

3.1.1. *Determining the Background*

The "background," the emission not due to M101, is composed of contributions from the instrumental/particle background, the X-ray emission from unresolved background active galactic nuclei (AGNs), the thermal emission due to the LHB, and the thermal emission due to the Galactic halo. The background may also contain contributions from truly diffuse extragalactic emission (see, e.g., Cen & Ostriker 1999).

We placed the nucleus of M101 near the aim point of the S3 chip and specified a roll angle so that the bulk of the $\frac{1}{4}$ keV emission observed by *ROSAT* would fill the S3 chip. The expectation was that the diffuse emission detected by *Chandra*, being significantly harder, would, like the *ROSAT* $\frac{3}{4}$ keV emission, cover a significantly smaller area and that the corners would be relatively free of contamination by M101, allowing a direct measurement of the background. Instead, we found that *Chandra's* greater sensitivity allows one to trace that emission at least to the edge of the chip in almost every direction. We have extracted a spectrum from the regions with the lowest surface brightness and find it to be consistent with models of what the background should be, and we adopt it as the true background.

In Figure 1 the three irregular polygons indicate regions with "low" surface brightness between strong spiral arms. The three regions contain statistically identical spectra. The mean spectrum from these regions, after the removal of the instrumental background (§ 3.2), is shown in Figure 3.

The instrumental background is due primarily to charged particles interacting with the detector CCDs and to X-rays produced by charged particles interacting with the structures around the CCDs. The instrumental background spectrum was derived from the "dark Moon" data and scaled to this observation using the background rate in the 10.5–14.5 keV region, where *Chandra* has an insignificant response to cosmic X-rays.

The dashed line in Figure 3 shows a model for the non-instrumental background calculated for a $5^\circ \times 5^\circ$ box in the direction of M101 from the *ROSAT* All-Sky Survey (RASS) using the method of Kuntz & Snowden (2000). The extragalactic background (*dotted line*), due to unresolved background AGNs, is modeled by a power law of index 1.46 and

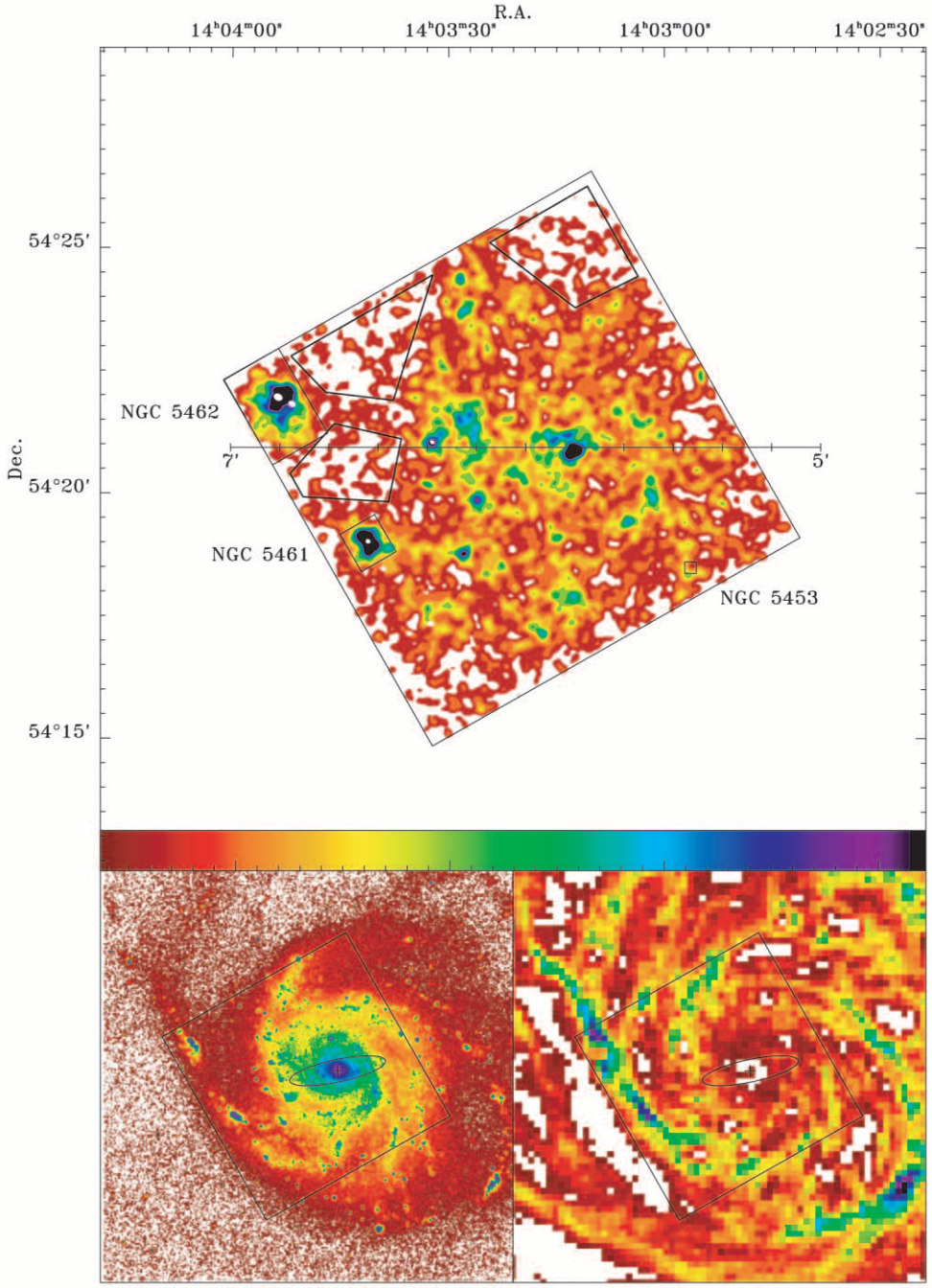

FIG. 1.—*Top*: X-ray image of M101 in the 0.45–1.0 keV interval after point-source removal, smoothed by a Gaussian with an FWHM of 7.″9 (16 pixels). The color intervals are 1.6×10^{-6} counts cm^{-2} s^{-1} arcmin^{-2}, starting at the value of the background. White regions surrounded by high surface brightness regions denote the removal of bright point sources. The irregular polygons mark the regions used to determine the background. The rule is marked in arcminutes from the nucleus. *Bottom left*: Optical image from the Digital Sky Survey, with the position of the S3 chip marked. The ellipse marks the size and position of the large-scale CO bar. *Bottom right*: H I 21 cm image from Kamphuis (1993). The color scale runs from 10^{20} (*white*) to 2×10^{21} cm^{-2}.

a normalization of 10.5 keV cm^{-2} s^{-1} sr^{-1} keV^{-1} (Chen, Fabian, & Gendreau 1997). This normalization includes emission from sources brighter than our point-source detection limit; to remove the flux due to sources brighter than our detection limit, we used the model of Mushotzky et al. (2000). The extragalactic emission was then absorbed by the disk of M101 ($\sim 4.4 \times 10^{20}$ cm^{-2}).

The Galactic foreground model contains contributions from the LHB (whose contribution is unabsorbed) and a two–thermal component Galactic halo, which is absorbed by 9×10^{19} cm^{-2}, the Galactic column in the direction of M101. Since the Raymond & Smith (1977) model temperature for the LHB is well constrained by a series of *ROSAT* observations (Snowden et al. 1998, 2000; Kuntz & Snowden 2000), that parameter was fixed to $T = 10^{6.11}$ K ($kT = 0.111$ keV) in the RASS fits, but all the other parameters were allowed to vary. The solid line shows the best fit of this model to the *Chandra* data for the low surface brightness regions. It is not known whether the harder Galactic halo component is truly Galactic, or whether it may be, in part, extragalactic. Assuming that it is extragalactic and absorbed by the M101 disk reduces the transmitted flux by only 4%.

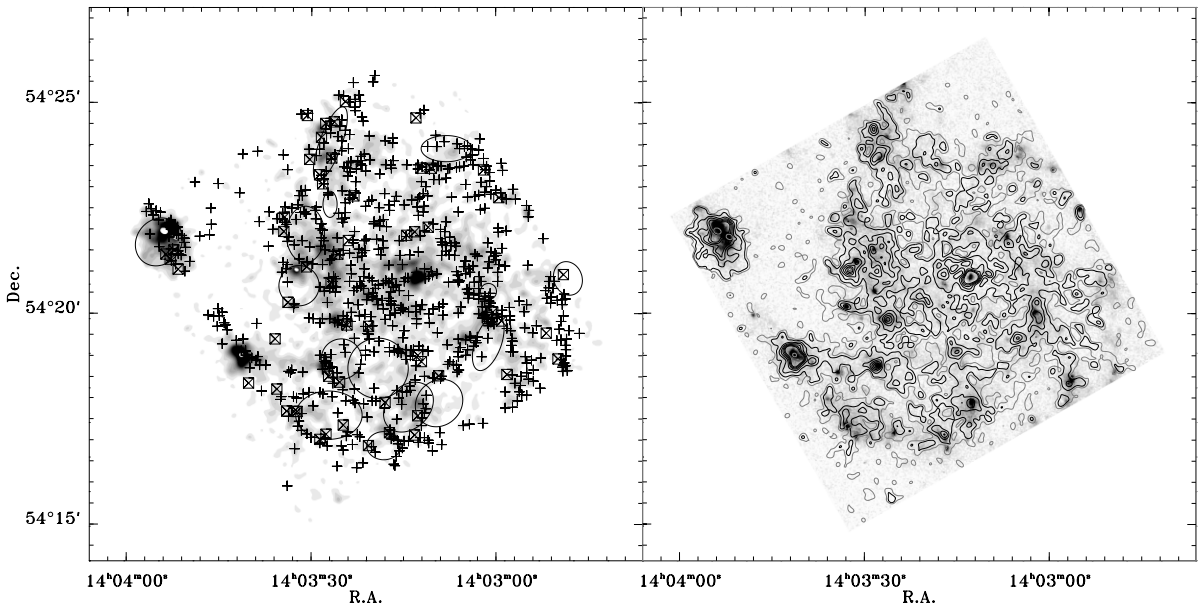

FIG. 2.—*Left*: Diffuse X-ray emission in M101 overlaid on the H II regions from Hodge et al. (1990; *crosses*), the H I holes listed by Kamphuis (1993; *ellipses*), and the SNR of Matonick & Fesen (1997; *boxes*). *Right*: UIT image (*gray scale*) compared to the X-ray image (*contours*). The dark X-ray contours are $(1, 2, 3, 4, 5, 6) \times 3.2 \times 10^{-6}$ counts cm^{-2} s^{-1} arcmin^{-2}, corresponding to one contour for each two color steps in the X-ray image of Fig. 1. The light X-ray contour is 1.6×10^{-6} counts cm^{-2} s^{-1} arcmin^{-2}.

Above 2 keV, these low-temperature thermal spectra have virtually no flux, yet the data contain significant flux in the 2–5 keV interval. This 2–5 keV flux is due almost entirely to the instrumental background from unremoved low-level background flares. By comparing the instrumental background spectra in the observation of GK Per during periods with and without flares, one can show that the instrumental background during flares has a power-law shape, without convolution with the response function. We have assumed that the spectral shape of low-level flares is similar to that of the stronger flares. To remove the residual low-level flares from the M101 observation, the 2–5 keV interval was fitted with an unconvolved power law and those parameters transferred to the fits in the 0.45–2.0 keV interval. The solid lines contain the result of this fit to the 2–5 keV interval.

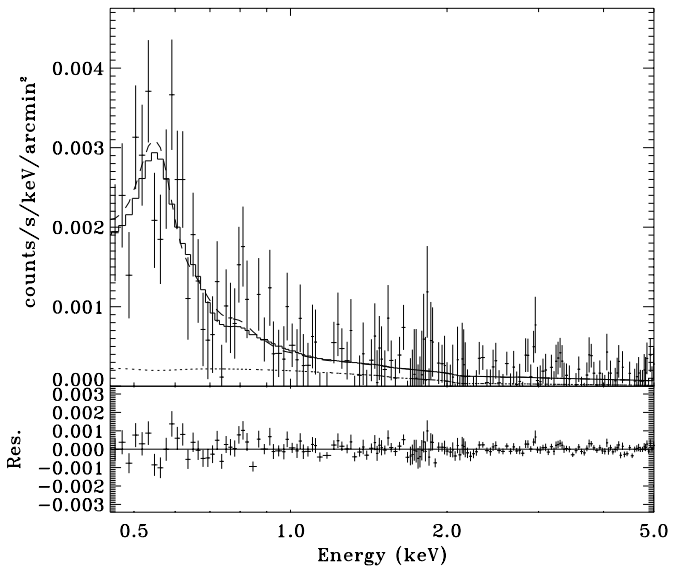

FIG. 3.—Spectrum in the background regions. The dashed line shows the best *ROSAT* model, and the solid histogram shows the best-fit *Chandra* model. The dotted line shows contribution by the unresolved background sources.

Figure 3 demonstrates that the *ROSAT* model for the Galactic foregrounds in the direction of M101 produces a spectrum similar to that seen in the regions between the arms of M101, with nearly the same normalization. The best-fit model to the *Chandra* data produces 77.8×10^{-6} counts s^{-1} arcmin^{-2} in *ROSAT* band R45, while the RASS contains $(81.8 \pm 4.2) \times 10^{-6}$ counts s^{-1} arcmin^{-2} for a square degree surrounding, but not including, M101. Thus, the low surface brightness interarm regions from which these spectra were derived appear to have very little contamination by emission from M101 itself. We have used this spectrum as the Galactic foreground spectrum.

3.1.2. *Surface Brightness and Total Flux*

The radial profile of the 0.45–1.0 keV emission is shown in Figure 4. As might be expected, the two giant H II regions produce large perturbations to the radial distribution. Without the contribution of the giant H II regions, the X-ray exponential scale length is 5.24 ± 0.49 kpc, similar to the scale lengths in both the V band, $R_V = 5.19$ kpc, and the B band, $R_B = 5.40$ kpc (Okamura, Kanazawa, & Kodaira 1976).

Excluding the giant H II regions, the total flux within a radius of 10 kpc is 1.5×10^{-4} counts cm^{-2} s^{-1} in 0.45–1.0 keV. The giant H II regions provide an additional 0.22×10^{-4} counts cm^{-2} s^{-1} in 0.45–1.0 keV. Since the flux is dominated by the low surface brightness regions, we used the spectrum of the low surface brightness gas to find a conversion to physical units of 1.61×10^{-9} ergs count^{-1}, and thus a total 0.45–1.0 keV luminosity of 1.70×10^{39} ergs s^{-1}. Within a radius of 10 kpc, the total luminosity of point sources (other than P98) is 0.68×10^{39} ergs s^{-1} in 0.45–1.0 keV.

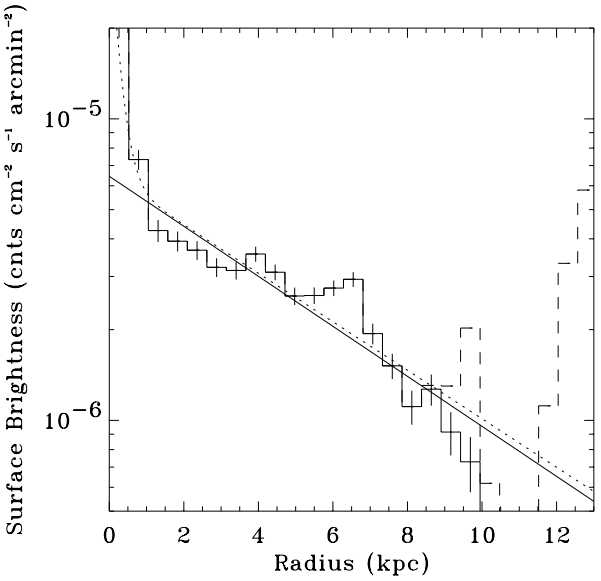

FIG. 4.—The 0.45–1.0 keV X-ray surface brightness as a function of radius. The solid histogram excludes the giant H II regions; the dashed histogram includes the giant H II regions. The solid line shows the fitted exponential. The dotted line shows the optical profile from Okamura et al. (1976) scaled to the same central surface brightness for the exponential disk.

Extrapolating the exponential relation shown in Figure 4, assuming a $\Gamma = 1.6$ spectrum for the point sources, and adding the flux due to the nuclear region and the giant H II regions, we find a luminosity of 3.16×10^{39} ergs s^{-1} within the central 7.5 in the 0.45–1.0 keV interval and 3.58×10^{39} ergs s^{-1} in the 0.44–1.21 keV interval. This value compares well to the 3.6×10^{39} ergs s^{-1} found by *ROSAT* in the same region in the 0.44–1.21 keV interval (Snowden & Pietsch 1995), further implying that about 40% of the "diffuse" *ROSAT* flux was due to unresolved point sources.

3.1.3. *Color Gradients*

A brief glance at the spectra in following sections reveals that the emission in the 0.45–2.0 keV interval is dominated by O VII (0.560 keV), O VIII (0.650 keV), and a complex of iron lines in the 0.7–1.0 keV interval. For a first-order understanding of the diffuse emission, we considered the (0.70–1.0 keV)/(0.45–0.70 keV) hardness ratio. Because the count rate is low and the counting statistics poor, we present the hardness ratio as functions of radius and surface brightness (Fig. 5) rather than as a map. The hardness ratio is constant at low surface brightnesses (below $\sim 10^{-5}$ counts cm^{-2} s^{-1} arcmin^{-2}). In the surface brightness interval $(1.3–1.8) \times 10^{-5}$ counts cm^{-2} s^{-1} arcmin^{-2} the hardness ratio is much higher. However, the bulk of this emission comes from a limited number of compact, bright emission regions, some of which are identified as H II regions (Hodge et al. 1990). Above 2×10^{-5} counts cm^{-2} s^{-1} arcmin^{-2}, the emission comes from the nucleus and the giant H II regions. There is a slight and statistically insignificant increase of hardness with surface brightness for the nucleus and a greater increase (although still statistically insignificant) for the giant H II regions. There is no statistically significant trend of hardness with radius.

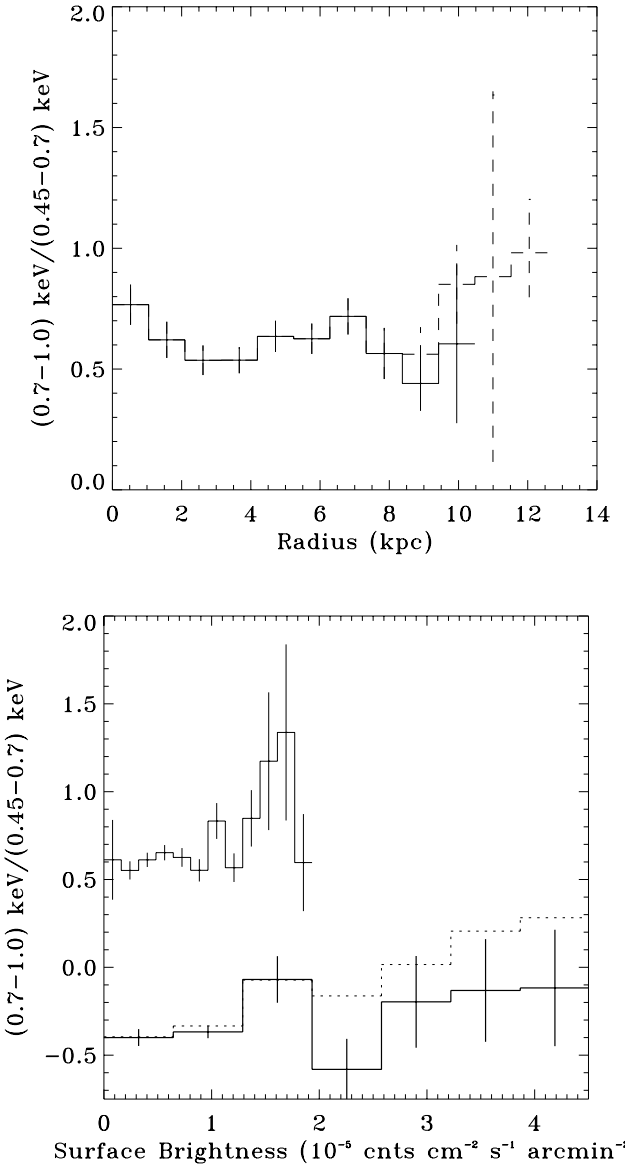

FIG. 5.—*Top*: Hardness ratio as a function of radius. The solid line excludes the giant H II regions; the dashed line includes the giant H II regions. *Bottom*: Hardness ratio as a function of surface brightness. The lower histogram is more broadly binned and is offset in color by −1. The upper histogram above 1.3×10^{-5} counts cm^{-2} s^{-1} arcmin^{-2} is dominated by a small number of bright knots.

3.2. *Spectroscopy*

As noted in § 3.1.1, the background spectrum contains contributions from the Galactic foregrounds (the LHB and the Galactic halo), the extragalactic background, and the instrumental/particle background.

The Galactic foreground/extragalactic background spectrum was derived from the background regions noted in § 3.1.1. The ratio of the response in the region covered by M101's diffuse emission to the response in the background region is energy dependent and can vary from 1% to 5% over 100 eV. Since the instrumental background is patterned,[3] the instrumental background spectrum will not scale with

[3] See Markevitch (2001) at http://cxc.harvard.edu/contrib/maxim/bg/index.html.

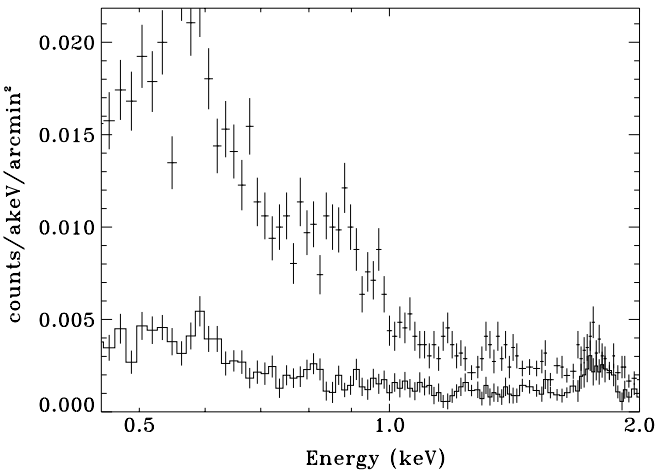

FIG. 6.—Raw spectrum of the diffuse emission. The lower spectrum shows the background. Features at 1.2 and 1.38 keV (see § 3.2) are apparent in the raw spectrum; the 1.2 keV feature may have been augmented by the background subtraction.

area. Therefore, in order to derive a background spectrum for some particular region of M101, we extracted the spectrum from the background regions and removed from it the appropriate instrumental background spectrum (isolating the cosmic background spectrum). We then scaled the spectrum by the ratios of the responses and areas for the appropriate regions, and added the correct instrumental background spectrum appropriate for the region of M101, propagating all uncertainties. Figure 6 shows a raw spectrum of the large-scale diffuse emission and its background, as computed by the method outlined above.

Since the exposure was made on day 247 after launch, the accumulating absorption thought to be due to organics condensing on the optical blocking filter is negligible.

We have used solar metallicities in the spectral fitting. The abundance gradient in M101 has been studied extensively using gas-phase abundances in H II regions (Garnett et al. 1999; Garnett & Kennicut 1994; Garnett 1989; Torres-Peimbert, Peimbert, & Fierro 1989; Evans 1986), yielding either abundance trends (He, N, O, S) or mean abundances (C, Ne, Ar). For the region covered by the *Chandra* observation, the abundances are close to solar for these elements. The nucleosynthetic studies of Timmes, Woosley, & Weaver (1995) and Alibés, Labay, & Canal (2001), which contain compendia of Galactic abundance data in the form of X/Fe as a function of Fe/H, can be used to link the observed species to those of interest for X-ray spectroscopy, e.g., Ca, Si, Fe, and Ni.

We have extracted spectra for three values of surface brightness, A: 1.6–4.8, B: 4.8–8.0, and C: (8.0–11.2) $\times 10^{-6}$ counts cm^{-2} s^{-1} arcmin^{-2} (where the values are above the nominal background). These spectra are shown in Figure 7.

With the exception of features at 1.2 and 1.38 keV (discussed further below), spectra A and B are well fitted with two thermal components, using MEKAL models (Liedahl, Osterheld, & Goldstein 1995; Mewe, Lemen, & van den Oord 1986; Mewe, Gronenschild, & van den Oord 1985). Spectrum C can also be fitted by the same model, but the significantly smaller number of counts produces a less significant fit. That the spectra are fitted by two thermal components is not surprising. In the 0.45–1.0 keV interval, there

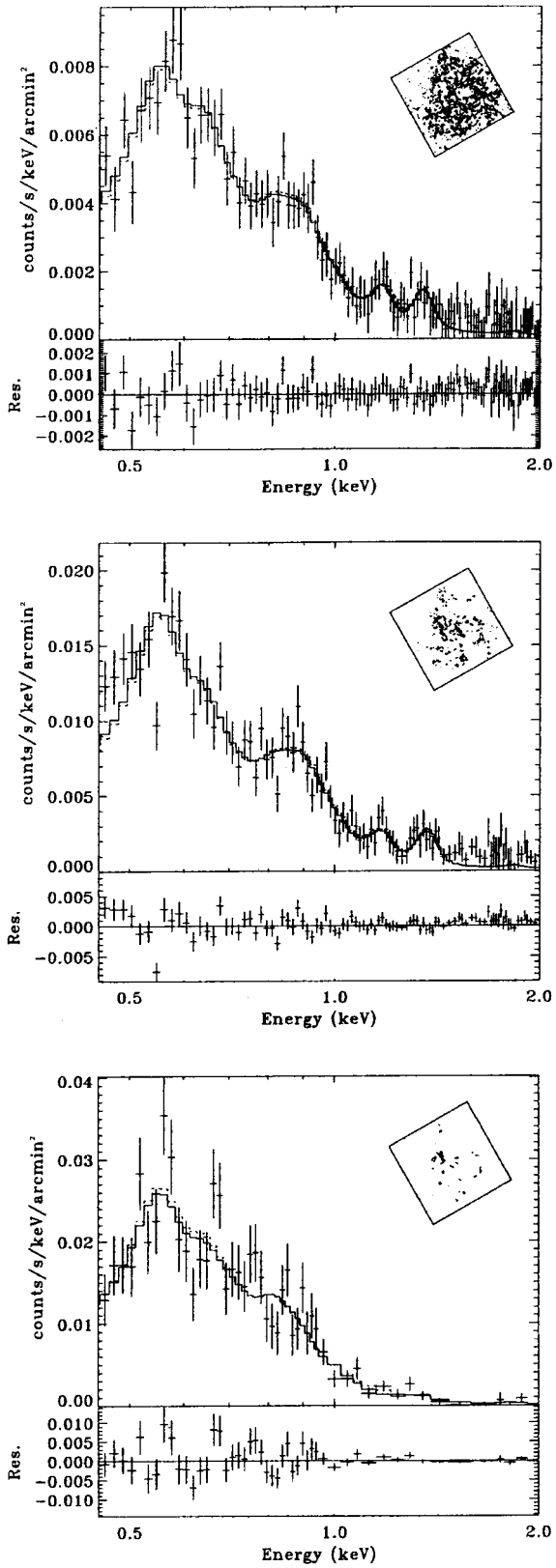

FIG. 7.—*Top*: Spectrum A, the spectrum for regions with surface brightness (1.6–4.8) $\times 10^{-6}$ counts cm^{-2} s^{-1} arcmin^{-2}. The solid line shows the fit assuming no internal absorption; the dotted line shows the fit assuming that half of the emission is behind the full absorbing column of the disk. The inset shows the region from which the spectrum was extracted. The features at 1.2 and 1.38 keV were modeled as zero-width Gaussians. *Middle*: Spectrum B, the spectrum for regions with surface brightness (4.8–8.0) $\times 10^{-6}$ counts cm^{-2} s^{-1} arcmin^{-2}. *Bottom*: Spectrum C, the spectrum for regions with surface brightness (8.0–11.2) $\times 10^{-6}$ counts cm^{-2} s^{-1} arcmin^{-2}.

TABLE 2
SPECTRAL FIT PARAMETERS: LARGE-SCALE DIFFUSION EMISSION

Spectrum	Counts[a]	$\overline{R}$ (kpc)	N_H[b] ($\times 10^{20}$ cm^{-2})	T_S (kT)	EM$_S$ ($\times 10^{-2}$ cm^{-6} pc)	T_H (kT)	EM$_H$ ($\times 10^{-3}$ cm^{-6} pc)	χ_ν	ν
A	12907/5582	5.64	0.0	0.210 ± 0.015	1.75 ± 0.17	0.741 ± 0.048	5.94 ± 1.06	0.71	97
			0.0, 3.2	0.203 ± 0.013	1.31 ± 0.11	0.730 ± 0.080	3.46 ± 0.54	0.71	97
B	4459/1231	4.80	0.0	0.195 ± 0.010	3.72 ± 0.28	0.754 ± 0.066	13.3 ± 0.2	1.56	85
			0.0, 14.2	0.190 ± 0.009	2.87 ± 0.20	0.752 ± 0.073	7.77 ± 0.97	1.55	85
C	1442/315	4.76	0.0	0.197 ± 0.021	5.66 ± 0.67	0.607 ± 0.117	17.6 ± 0.6	1.36	43
			0.0, 15.4	0.194 ± 0.018	4.58 ± 0.63	0.599 ± 0.101	9.95 ± 0.47	1.37	43
A+B	17366/6813	5.49	0.0	0.204 ± 0.010	2.11 ± 0.14	0.746 ± 0.060	7.56 ± 0.91	0.85	97
			0.0, 13.1	0.198 ± 0.012	1.59 ± 0.11	0.732 ± 0.064	4.23 ± 0.54	0.86	97
ROSAT[c]	23872/16640	7.03	0.0	0.215 ± 0.028	0.745 ± 0.135	0.695 ± 0.210	1.35 ± 1.14	0.55	99
			0.0, 10.6	0.210 ± 0.025	0.540 ± 0.082	0.691 ± 0.237	0.704 ± 0.576	0.55	99
Extended nucleus	794/276	1.12	0.0	0.198 ± 0.026	3.48 ± 0.54	0.706 ± 0.126	8.53 ± 3.56	1.07	32
			0.0, 23.3	0.196 ± 0.019	3.06 ± 0.48	0.711 ± 0.153	4.74 ± 2.84	1.10	32

NOTE.—For any given spectrum, the first line contains the fit assuming all emission to be on the surface of the disk, and the second line contains the fit assuming that half of the emission is behind the entire absorbing column of the disk. The two values of the column density denote the absorption applied to each half of the emission. All uncertainties are 90% confidence intervals.

[a] The first number is the number of raw counts in 0.45–2.0 keV, and the second number is the calculated number of particle background counts in the same energy interval.

[b] The column density of hydrogen atoms in the H I and H_2 components. This quantity should be roughly proportional to the column density of X-ray absorbers. For all fits, the absorbing column was fixed. The absorption listed here is exclusive of the 9×10^{19} cm^{-2} due to the Milky Way.

[c] Region used for comparison with *ROSAT*.

are three major features to be fitted: the O VII 0.56 keV line, the O VIII 0.65 keV line, and the 0.7–1.0 keV complex of Fe lines. The Fe complex dominates the fit of the harder component, while the O VII/O VIII ratio dominates the fit of the softer. Our simplest model does not include the effect of absorption internal to M101. A trial fit in which the absorption for each component was allowed to vary independently found no absorption for the soft component. The absorption for the hard component was, understandably, poorly determined, with the uncertainty being nearly as large as the fitted value, $\sim 3 \times 10^{21}$ cm^{-2}.

After fitting the two thermal components, there remained two further features at 1.2 and 1.38 keV, as well as a small amount of flux below 1.65 keV. Above 1.65 keV, the Si Kα line from the particle background, although well removed, substantially increases the uncertainty. Above 2.0 keV there is no significant flux. Examination of Figure 6 shows that, while the 1.2 keV feature may be augmented by poor background subtraction, neither feature is produced by the background subtraction process. Nonequilibrium models were no more adequate for fitting these lines than MEKAL models. Because of the small number of counts in this energy interval, the spatial distribution of this contribution can be determined only from very heavily smoothed images (FWHM $\sim 32''$). The distribution of the 1.1–1.65 keV emission is poorly correlated with the 0.45–1.0 keV emission, which contains the bulk of the galactic emission. Although 1.1–1.65 keV emission is typically found where the 0.45–1.0 keV emission is strong, it is also found where there is little 0.45–1.0 keV emission. The 1.1–1.65 keV emission is not correlated with the 2.5–5.0 keV emission, which should contain no galactic emission and should be composed primarily of the particle background; nor is the 1.1–1.65 keV emission correlated with the 2.5–5.0 keV either. Since there is no obvious astrophysical justification for these features and they are relatively faint compared to the total flux, we have arbitrarily modeled them as unresolved lines, i.e., Gaussians with only instrumental broadening, whose amplitude and energy were free to vary.

In order to estimate the effects of internal absorption on the spectral parameters, we fitted the spectra assuming both no internal absorption and that half of the emission is behind the disk absorption. The fit parameters are listed in Table 2. The map of the total absorbing column was constructed from the $30''$ resolution H I map of Kamphuis (1993) and a $55''$ resolution CO map from the Berkeley-Illinois-Maryland Array Survey of Nearby Galaxies (Helfer et al. 2003). A map of the total absorbing column density is shown in Figure 8. The CO map does not cover the entire area observed by *Chandra*, but does cover the area containing the bulk of the emission. A model assuming that half of the emission is behind the absorption due to the M101 disk typically reduces the temperature of the soft component by $\sim$0.005 keV, increases the total soft emission measure by $\sim$87%, reduces the temperature of the hard component by $\sim$0.009 keV, and increases the total hard emission measure by $\sim$60%.

The temperature of the soft component is similar to that found by Wang et al. (1999; 0.186 keV) from a joint *ROSAT* PSPC–*ASCA* GIS fit. Likely as a result of a factor of $\sim$3 better spectral resolution for the *Chandra* data, we do not see evidence for their hotter component ($kT \geq 5.1$ keV), and fixing our hard component to $kT = 5.1$ keV produces a significantly poorer fit ($\Delta\chi^2 = 28$).

3.2.1. *Joint Fits with ROSAT*

Given that *ROSAT* has a much stronger soft response and that softer components could contribute to the O VII emission, these softer components, not visible to *Chandra*, could change the temperatures of the components fitted to the *Chandra* spectrum. Therefore, we attempted to determine whether the *Chandra* fit was, in fact, consistent with the *ROSAT* data.

From the *ROSAT* data we extracted the region covered by the *Chandra* chip S3, but not including the giant H II regions or a small region around the nucleus. The background was derived from an annulus between $25'$ and $50'$,

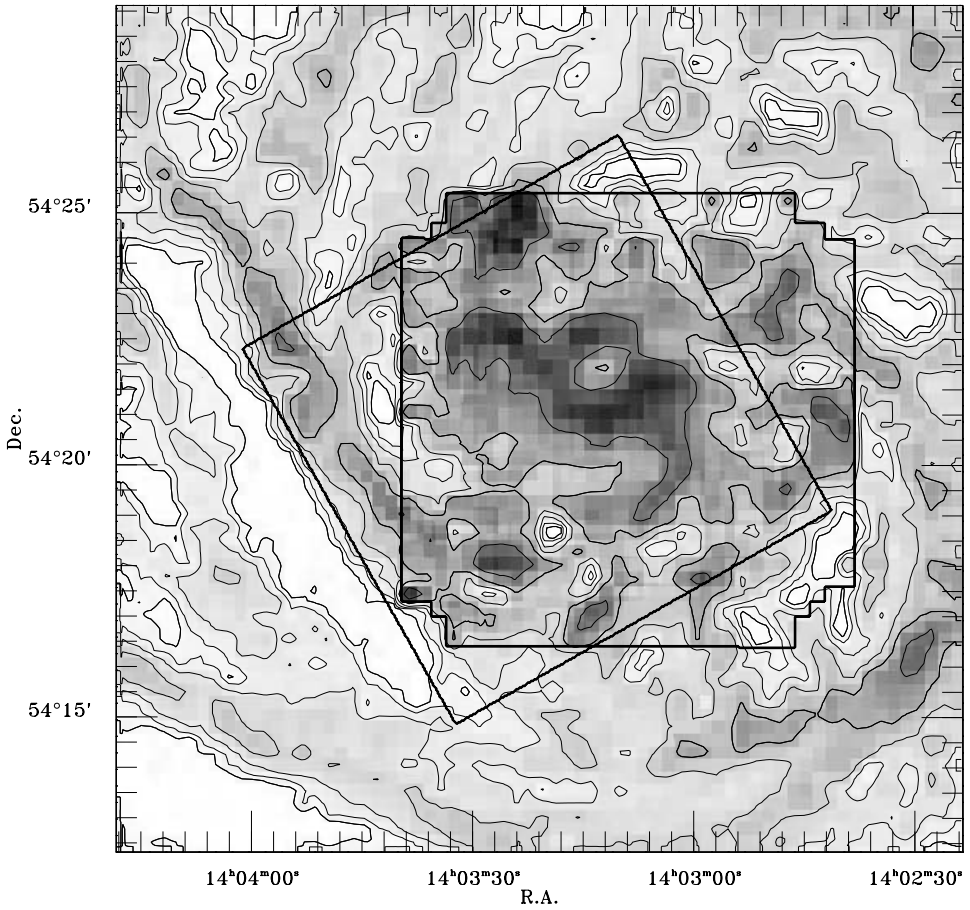

FIG. 8.—Total absorbing column. The contours are logarithmic from 10^{20} to 3.2×10^{21} cm^{-2} in steps of $10^{0.25}$. The heavy lines show the location of the *Chandra* image and the area covered by the CO map. With the exception of the giant H II regions, the bulk of the region containing X-ray emission is covered by the CO map.

beyond the observed M101 emission. The raw source spectrum contained 3769 counts, of which 2538 were due to the particle background and Galactic foreground. The comparable *Chandra* spectrum was created in two parts. First, we extracted and fitted the spectrum for all of the regions containing point sources, excluding source P98 (since P98 is brighter than all of the other point sources combined and was clearly not visible during the *ROSAT* exposure). The point-source contribution was reasonably well modeled by a power law with $\Gamma = 1.6$ and $N_{\rm H} = 4 \times 10^{20}$ cm^{-2}. Second, we extracted and fitted the diffuse emission from the remainder of the chip, excluding the point sources, the giant H II regions, and a small region around the nucleus. For both the *Chandra* and *ROSAT* spectra, the contribution of the unresolved extragalactic background was calculated and removed.

The combined model is shown in Figure 9. The normalization of the *Chandra* model above the carbon edge (primarily the contribution from the diffuse emission) appears to be slightly too high, but within the uncertainties of the individual data points. Below the carbon edge (*ROSAT* bands R1 and R2, the $\frac{1}{4}$ keV emission), the emission is split nearly evenly between point sources and the diffuse component. There remains significant emission below the carbon edge that is not accounted for by the *Chandra* model. In joint fits of the *ROSAT* and *Chandra* data, the temperature of the soft *Chandra* component remained well constrained, but neither the very soft component seen only by *ROSAT* nor the harder *Chandra* component were well constrained. Assuming that the fit to the *Chandra* spectra was a good model of reality, we fitted the very soft component in the *ROSAT* data and found the 90% confidence interval to be $kT < 0.053$ ($\log T = 5.79$) and the 68% confidence interval for the normalization to include zero.

Given the small number of counts, the difficulty of background subtraction below the carbon edge, and the uncertainty of the *ROSAT* calibration at the extreme low energy boundary, one can confidently state only that there appears to be some excess emission below 0.35 keV. One cannot completely eliminate the possibility that the softer component seen by *Chandra* does, in fact, contain contributions by even softer components. The similarity of the upper limit of the very soft component to the temperature derived by Snowden & Pietsch (1995) from the *ROSAT* R2/R1 band ratio is surprising and likely coincidental, given that such a large portion of the $\frac{1}{4}$ keV emission is due to point sources (§ 3.1.2).

4. SMALL-SCALE DIFFUSE EMISSION

4.1. *Nucleus/Bulge*

M101 has a large-scale bar in CO ($J = 1 \rightarrow 0$) emission (Kenney, Scoville, & Wilson 1991), which is marked in Figure 1. It has a position angle of $102^\circ \pm 4^\circ$ and a length of $1\farcm5 \pm 0\farcm5$ and appears to "anchor" the main optically

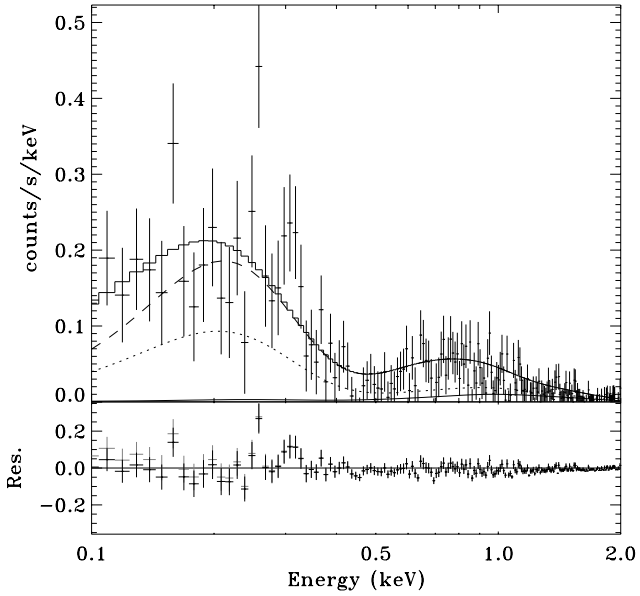

FIG. 9.—*ROSAT* spectrum of the region covered by the *Chandra* S3 chip. The smooth solid line is the contribution by the unresolved extragalactic background. The dotted line shows the contribution by the point sources detected in the *Chandra* image. The dashed line shows the sum of the *Chandra* model of the diffuse emission and the previous two components. The stepped solid line shows the previous spectrum with the addition of the fitted "*ROSAT* component." The residuals plotted are from the fit containing the *ROSAT* component. The gray residuals are from the *Chandra* model alone.

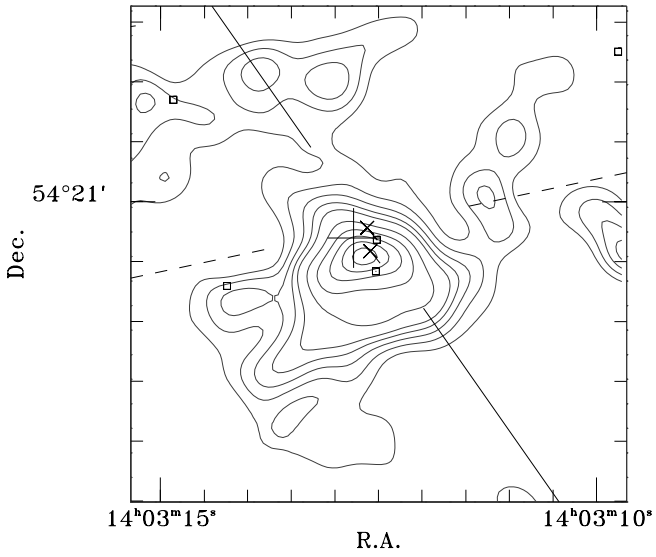

FIG. 10.—Nuclear region. The X-ray contours are (1, 1.5, 2.0, 2.5, 3, 4, 5, 6, 7, 8) $\times 10^{-5}$ counts cm^{-2} s^{-1} arcmin^{-2}. The image has been smoothed by a 3.″97 FWHM Gaussian. The solid straight line shows the line of nodes; the northwest corner is toward the observer. The dashed straight line shows the orientation of the molecular bar. The cross shows the location and uncertainty of the Israel et al. (1975) position of the radio continuum nucleus. The upper × shows the position of the optical nucleus from a WFPC1 image; the lower × shows the position of the southern optical/Hα source. The small boxes show the X-ray point sources. The nonsystematic uncertainties of the positions of the optical and X-ray sources are much smaller than the plot symbols.

defined inner arms. At higher resolution (2″), M101 is a classic "twin-peak" source, showing strong CO emission from two compact regions flanking the nucleus where the flow of molecular gas down the bar crosses the inner Lindblad resonance (Kenney et al. 1992). The two peaks are separated by $\sim$3.″5 and have a position angle of roughly $-10°$. The CO images show filaments stretching from the twin peaks outward, roughly along the bar.[4] There is no CO concentration associated with the nucleus.

A similar morphology is seen in Hα (Moody et al. 1995). The (presumed) nucleus is bright in Hα and is flanked by two peaks of emission $2.''4 \pm 0.''15$ from the nucleus (farther out than the CO peaks) at a position angle of $+10°$. A strong Hα filament coincides with the southern CO filament, and some Hα features coincide with an extension of the northern CO filament. A *Hubble Space Telescope* (*HST*) Wide-Field Planetary Camera 1 (WFPC1) image (5479 Å) on PC chip 6 shows a bright pointlike source at the position of the southern Hα peak but no northern counterpart (Moody et al. 1995).

Figure 10 shows the nuclear region of our *Chandra* observation smoothed by a 1.″968 (four ACIS pixels) half-width at half-maximum Gaussian. Pence et al. (2001) used optical SNRs to tie the X-ray coordinate system to the optical coordinate system of Matonick & Fesen (1997) and found that the *Chandra* coordinates need be corrected by an offset of $0.''47 \pm 0.''20$, which is less than the size of an ACIS pixel. The boxes in Figure 10 mark X-ray point sources; the position uncertainties are significantly smaller than the marked boxes. The separation of the two nuclear sources is 3.″16.

[4] Note that the position angle of the bar described in Kenney et al. (1991) is rotated by $\sim$25° from the bar described in Kenney et al. (1992).

The large cross in Figure 10 marks the position and uncertainty of the continuum nuclear source (Israel, Goss, & Allen 1975) and the dynamical center determined from the CO (Kenney et al. 1991). The upper × marks the optical nucleus, and the lower × marks the southern optical/Hα source. The nonsystematic uncertainty for the optical sources is also very small on this figure. Both of the optical sources, the northern X-ray source, and the peak of the diffuse X-ray emission are within the positional uncertainty for the continuum nucleus. The long tails on the optical symbols show the shift necessary to make the optical nucleus coincide with the northern X-ray source; if the northern X-ray source is the optical nucleus, the southern X-ray source does not coincide with the southern Hα source.

Since both the northern and southern nuclear X-ray sources have spectra consistent with those of rather ordinary X-ray binaries, their locations may be coincidental. This region is dynamically interesting and might be expected to shed light on the complex occurrences at the center of our own Galaxy. If we take the *HST* and *Chandra* astrometry at face value, the bulk of the diffuse X-ray emission from the nuclear region is centered near the southern optical/Hα source, which, given its proximity to the CO peak, might be expected to be a region of intense star formation. Given the extended nature of the emission and the position of the line of nodes, the lack of a northern counterpart is curious. Conversely, a $\sim$1.″5 shift, somewhat larger than the expected *HST*/*Chandra* rms offset ($\lesssim$1.″2), could make the optical nucleus coincident with the northern X-ray source.

Our understanding of the nucleus is hampered by the lack of a good independent measure of the offset in the optical and X-ray coordinate systems. This measure will come with

the execution of a survey of M101 with the *HST* Advanced Camera for Surveys in 2002 November, which will attempt to identify the X-ray sources over the entire ACIS-S3 field with optical counterparts.

4.1.1. *Spectroscopy*

We extracted spectra from the nuclear region at two different surface brightness levels. From the compact nucleus itself we extracted the region with surface brightness greater than 1.7×10^{-5} counts cm^{-2} s^{-1} arcmin^{-2}, shown by the higher thick contour in Figure 11. The mean column density for this region is 2.8×10^{21} cm^{-2}, the bulk of which (2.6×10^{21} cm^{-2}) is due to molecular gas. Although the nucleus itself is quite bright, the total number of counts is still small (239 counts in 0.11 arcmin^2). The spectrum is reasonably fitted by an absorbed bremsstrahlung, $N_{\rm H} = 1.8 \times 10^{21}$ cm^{-2}, $kT = 0.262$ keV, and $\chi_\nu = 0.58$ for $\nu = 10$ (Fig. 11, middle). Other spectral forms (power law, thermal plasmas, etc.) produced worse fits.

We extracted the spectrum of the extended emission around the nucleus, the region with surface brightness 0.725×10^{-5} counts cm^{-2} s^{-1} arcmin^{-2} $< S < 1.7 \times 10^{-5}$ counts cm^{-2} s^{-1} arcmin^{-2} between the two thick contours in Figure 11. The mean column density for this region is 2.3×10^{21} cm^{-2}, the bulk of which (2.2×10^{21} cm^{-2}) is due to molecular gas. This spectrum (Fig. 11, bottom) can be fitted with a two thermal components (see the "Extended nucleus" line in Table 2). Although we allowed the absorption to vary independently for the components, the fitted absorption was consistent with no absorption for either component. Including a bremsstrahlung component as a contaminant from the nucleus changes the thermal temperature and reduces the normalizations, but only slightly.

Thus, since the nuclear emission appears to be absorbed by about half of the total column density, it seems reasonable that the nucleus itself is embedded in the molecular ISM of the bar. The extended nuclear emission appears to be mostly unabsorbed and is likely extraplanar. Assuming that half of the extended nuclear emission is behind the column density measured in H I and CO does not significantly change the goodness of the fits or the fitted temperatures.

4.2. *Giant* H II *Regions*

Three giant H II regions fall on the S3 chip (see Fig. 1). Of these, NGC 5453 was not detected by either the *ROSAT* PSPC (Williams & Chu 1995) or the HRI (Wang et al. 1999) surveys. In this *Chandra* image there is a very faint enhancement partially encircling the listed position. NGC 5462 falls on the part of the chip with the worst PSF, and the PSF for NGC 5461 is only slightly better.

Both NGC 5461 and NGC 5462 were studied by Williams & Chu (1995), who found them resolved by the PSPC, but because of contamination by the soft extended disk emission, they could not rule out the presence of a single large X-ray source producing the X-ray emission from each region. Despite the relative softness of H II regions, both of these objects show extended emission in the deep HRI survey by Wang et al. (1999). In the *Chandra* image, both NGC 5461 and NGC 5462 show diffuse extended emission as well as bright point sources.

NGC 5462.—The spectrum was extracted from a region with a surface brightness greater than 3.3×10^{-6} counts

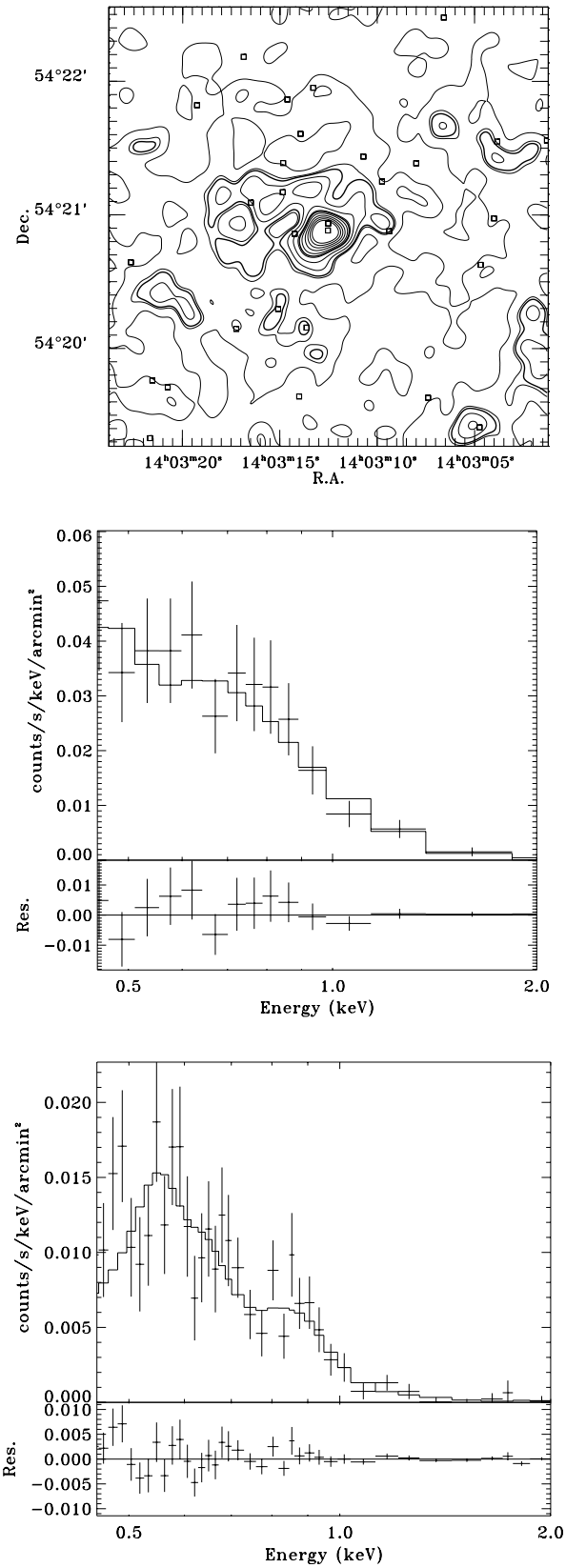

FIG. 11.—*Top*: Extended nuclear region. The smoothing is the same as in Fig. 1 (twice as much as in Fig. 10). The contours are from 0.32×10^{-5} to 3.2×10^{-5} counts cm^{-2} s^{-1} arcmin^{-2} in steps of 0.32×10^{-5}. The dark contours at 0.725 and 1.7×10^{-5} counts cm^{-2} s^{-1} arcmin^{-2} delimit the regions from which spectra were extracted. *Middle*: Spectrum for the region with surface brightness greater than 1.7×10^{-5} counts cm^{-2} s^{-1} arcmin^{-2}. *Bottom*: Spectrum for the region with 7.25×10^{-6} counts cm^{-2} s^{-1} arcmin^{-2} $< S < 1.7 \times 10^{-5}$ counts cm^{-2} s^{-1} arcmin^{-2}.

TABLE 3
SPECTRAL FIT PARAMETERS: GIANT H II REGIONS

Region	Counts[a] (0.45–2.0) keV	Area (arcmin^2)	N_H ($\times 10^{20}$ cm^{-2})	T_1 (kT)	EM_1 (cm^{-6} pc)	N_H ($\times 10^{20}$ cm^{-2})	T_2 (kT)	EM_2 (cm^{-6} pc)	χ_ν	ν
NGC 5461....	706/149	0.607	65^{+7}_{-16}	$0.155^{+0.038}_{-0.014}$	$7.2^{+8.0}_{-5.7}$	...	...	...	1.58	29
			0.9*	$0.261^{+0.034}_{-0.219}$	$0.048^{+.005}_{-0.024}$	125^{+129}_{-49}	$0.178^{+0.406}_{-0.115}$	$10.0^{+4805}_{-9.9}$	1.23	27
NGC 5462....	1199/331	1.518	54^{+10}_{-8}	$0.175^{+0.013}_{-0.028}$	$1.8^{+4.2}_{-0.9}$	...	...	...	0.968	47
			0.9*	$0.241^{+0.026}_{-0.021}$	$0.033^{+0.006}_{-0.006}$	407^{+207}_{-294}	$0.654^{+0.351}_{-0.136}$	$0.043^{+0.036}_{-0.023}$	0.938	45

NOTE.—Quantities with asterisks are fixed. All uncertainties are 90% confidence intervals.
[a] The first number is the raw counts in 0.45–2.0 keV, and the second is the calculated number of particle background counts.

cm^{-2} s^{-1} arcmin^{-2}. The diffuse emission is reasonably fitted ($\chi^2_\nu = 0.97$) by an absorbed MEKAL model. The fit is shown in Figure 12 (*top*). A somewhat better fit ($\chi^2_\nu = 1.2$) can be found by assuming the sum of an unabsorbed thermal component and an absorbed thermal component, the same type of model that fits the disk emission (see Table 3). In this case, the temperature of the unabsorbed component is well constrained and similar to the soft disk component; the absorbed component is not well constrained, but is clearly hotter. A fit containing an unabsorbed MEKAL component and an absorbed power law is significantly worse, implying that the nonthermal component is small. Extracting a spectrum using a higher surface brightness cut did not significantly change the fits. The SNR SN 1951H is offset from the X-ray center, but is within the extended emission. Given that a giant H II region is likely to be formed of many different X-ray–emitting components (e.g., expanding hot stellar wind bubbles, SNRs, etc.) and given the small number of counts in this spectrum, the poorness of the fit is not surprising.

NGC 5461.—The diffuse emission is reasonably fitted ($\chi^2_\nu = 1.58$) by an absorbed MEKAL model. The fit is shown in Figure 12 (*bottom*). As with NGC 5462, a somewhat better fit ($\chi^2_\nu = 1.2$) can be found by assuming the sum of an unabsorbed thermal component and an absorbed thermal component, but the fit parameters are poorly constrained.

5. DISCUSSION

Observations such as those discussed in this paper stand at the curious intersection of disciplines: between the theory of galaxy formation and the classical study of the ISM, between processes dominated by the depth and shape of the dark matter potential and processes dominated by the dynamical mixing of the ISM by star formation. We attempt here to place these observations in the context of both disciplines and begin by comparing M101 to the well-known but not so well understood ISM laboratory that is the Milky Way.

M101 is larger than the Milky Way, having a D_{25} about twice that of the Galaxy, but it has only about half the mass of the Milky Way, although with a larger mass fraction in neutral gas (see Table 1). The far-infrared luminosity, a very crude measure of the star formation rate, is about the same as that estimated for the Galaxy, implying that the star formation rate per disk area is substantially lower in M101. Comparing M101, for which $L_{\rm FIR}/D^2_{25} = 1.37 \times 10^{40}$ ergs s^{-1} kpc^{-2}, to the list of that quantity for edge-on spiral

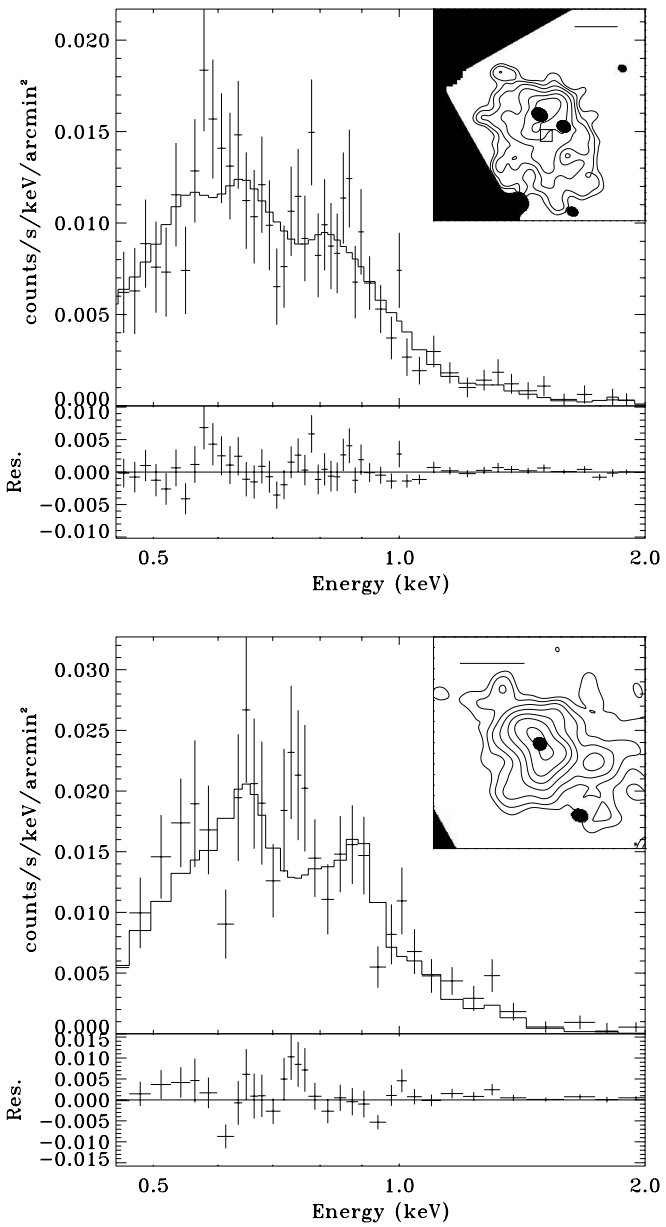

FIG. 12.—*Top*: Spectrum of NGC 5462. The model spectrum is the sum of an unabsorbed MEKAL thermal component and an absorbed MEKAL component. The inset image contours are (2.4, 4.0, 6.3, 10.0, 16.0, 24.0) $\times 10^{-6}$ counts cm^{-2} s^{-1} arcmin^{-2}. The black regions are either off-chip or removed for point sources. The scale bar is 30″ long. The box shows the location of SN 1951H. *Bottom*: Spectrum of NGC 5461. The model spectrum is an absorbed MEKAL thermal model.

galaxies from Rand (1998) and the correlation with extraplanar diffuse ionized gas, one can see that M101 is not expected to have a very extended "DIG" layer. This is not to say that star formation in M101 is in any way "quiescent"; the several giant H II regions are more reminiscent of those in the Magellanic Clouds than the star-forming regions seen in the Milky Way.

The M101 ISM may be quite similar to that of the Milky Way. Kregel, van der Kruit, & de Grijs (2002), using the work of Bottema (1993), have noted that the stellar velocity dispersion perpendicular to the disk is equivalent to the scaled circular $v_{\max}$. For spiral galaxies, the scale height of the old stellar population is nearly constant with radius (see, e.g., van der Kruit & Searle 1982). Thus, working from the optical *B*-band profile (Okamura et al. 1976), the H I rotation curve, and vertical velocity dispersion profile (Kamphuis 1993) and using the formulary of van der Kruit (1988), one can calculate the midplane density of the neutral gas and find $\rho_0 \sim 0.35$ cm^{-3} for the radii of interest (4–8 kpc). This value is similar to the midplane density of neutral gas in the solar neighborhood (0.22–0.38 cm^{-3}; Lockman & Gehman 1991). (The calculation uses the thin-disk approximation, which is valid for regions with a flat rotation curve; the rotation curve for M101 is gently rising at these radii, so the results must be viewed with some skepticism.) If one assumes that the M101 disk has a similar cold neutral medium/warm neutral medium/warm ionized medium structure as the Milky Way, then given the similar neutral gas density, one would expect the hot structures, if they are at all pressure-confined, to have properties similar to those in the Milky Way.

The prime difficulty with observing hot gas within the Milky Way is the high absorbing columns built up over lines of sight within the disk that limit our view of the Galaxy to the nearest 0.5–1.5 kpc at $0.5 < E < 1.0$, and to even shorter distances at lower energies. The filling factor of X-ray–emitting gas within the disk is thus a hotly debated topic. We know of several small isolated examples of bubbles of $\sim 10^6$ K gas (Snowden 2001) and one example of a superbubble filled with $\sim 2 \times 10^6$ K gas (Egger 1993). At higher energies, where we sample more of the Galactic disk, several hot Galactic ridge components have been identified (see, e.g., Kaneda et al. 1997, with $kT = 0.8$ and 7 keV), but their luminosities and filling factors are poorly known.

About our halo we know a little more. Using the *ROSAT* All-Sky Survey, Kuntz & Snowden (2000) divided the Galactic halo emission into two components, a hard component ($kT = 0.250^{+.079}_{-.045}$ keV), whose intensity remains constant across the high-latitude sky, and a patchy soft component ($kT = 0.098^{+0.055}_{-0.037}$ keV). (Whether these temperatures will survive the higher spectral resolution of the *Chandra* and *XMM-Newton* era is a topic of ongoing research.) The extraplanar X-ray emission from the Galactic bulge has been modeled as a cylinder of radius 5.6 kpc having an exponential scale height of 1.9 kpc and a temperature of $kT = 0.343$ keV (Snowden et al. 1997).

In M101, of course, we observe both disk and halo gas. Assuming that half of the emission is behind the absorption of the galactic disk, the total luminosity of diffuse emission is 1.53×10^{39} and 0.73×10^{39} ergs s^{-1} in 0.45–2.0 keV for the $kT = 0.2$ and 0.7 keV components, respectively. The total luminosity of these two components is $\sim$0.3% of the supernova luminosity, assuming two supernovae per century (Matonick & Fesen 1997).

The bulk of the emission observed by *Chandra* in the 0.45–1.0 keV energy interval is due to diffuse emission; only $\sim$6% of this observed diffuse emission is likely to be due to unresolved X-ray point sources such as X-ray binaries. This isolation of the emission due to point sources contrasts sharply with the *ROSAT* and *ASCA* observations, in which the luminosity function of the point-source population, and thus its contribution to the unresolved flux, was very poorly known. This study shows that some 40% of the 0.44–1.21 band flux measured by *ROSAT* was due to unresolved point sources, indicating that the measured *ROSAT* temperatures for M101 and similar objects should be viewed with caution. From the spectra of the diffuse emission, it is clear that the point-source contribution above 1 keV will be even greater. The term "diffuse" should be used with caution because, as will be seen in the following section, some fraction of that emission will be due to unresolved stars.

5.1. *Disk*

The bulk of the disk of M101 is covered by low surface brightness X-ray emission that traces the spiral arms. The low surface brightness emission in M101 appears to consist of two different components, and the constancy of the hardness ratio shows that the relative amounts of these two components is relatively constant for the bulk of the emission. This uniformity suggests that the sources of the two components are linked to one another and to star formation. A similar two-component medium is seen in the spectrum of the actively star-forming galaxy NGC 2403 (Scd), where the best-fit two–MEKAL component model has temperatures of $kT = 0.18 \pm 0.03$ and 0.73 ± 0.07 keV (Fraternali et al. 2002), while the early-type spiral NGC 1291 (Sa) appears to have a single thermal component with a temperature $kT = 0.33$ keV (Irwin, Sarazin, & Bregman 2002). As the diffuse emission is analyzed for similar galaxies in the *Chandra* and *XMM-Newton* archive, such two-component media may become a mark of late-type disks.

The softer component in M101 has a temperature of $\sim$0.2 keV. This is similar to the temperature found for superbubbles such as those in the Magellanic Clouds or that outlined by the Galactic Loop I. The brightest portion of the Loop I superbubble, a shock front seen obliquely, has $kT =$ 0.17–0.30 keV and an emission measure of 0.02–0.04 cm^{-6} pc (Egger & Aschenbach 1995). The emission measure of the softer component of the M101 disk is similar, 0.018–0.038 cm^{-6} pc, suggesting a covering fraction near unity for superbubbles, or, more reasonably, that a substantial amount of the gas is actually in the halo. An object similar to the Loop I superbubble (radius = 150 pc) would subtend an angle of 8.′6 at the distance of M101 and have a surface brightness of $\sim 3 \times 10^{-3}$ counts cm^{-2} s^{-1} arcmin^{-2}. Because of its small size, after the smoothing applied to produce the data shown in Figure 1, it would have a surface brightness of only $\sim 3 \times 10^{-6}$ counts cm^{-2} s^{-1} arcmin^{-2}. In the presence of other diffuse emission, the Loop I superbubble would be indistinguishable in the disk of M101.

It is interesting to note that unlike NGC 2403, where the sound speed of the softer component was comfortably below the escape speed, in M101 the sound speed of the softer component [$(\gamma kT/\mu m_p)^{1/2} \sim 230$ km s^{-1}] is just barely compatible with the escape velocity ($\sqrt{2}v_c \sim 240$ km s^{-1}). However, this simple comparison should not be taken as indicating that the gas is escaping the galaxy.

Breitschwerdt & Schmutzler (1999) modeled galactic chimney flows in a dynamically self-consistent manner and found that the adiabatic expansion of the gas out of the disk cools the gas significantly, but leaves a much higher, nonequilibrium ionization structure frozen into the gas. Their model starts with an initial collisional ionization equilibrium gas at 2.5×10^6 K, but the gas cools rapidly with increasing height above the disk to $\sim 10^4$ K and has a spectrum more similar to that of a 10^6 K gas. Given that the bulk of the temperature information for the soft component is derived from the ratio of the oxygen lines, our temperature may not indicate the true gas temperature, but only the ionization temperature of the oxygen.

Kahn (1991, 1998) has placed a more restrictive constraint on this gas. Calculations for the Galaxy show that the galactic chimney/fountain gas cools long before reaching the scale height indicated by its initial temperature, a result confirmed by the modeling of de Avillez (2000). Thus, the fountain gas is supported dynamically, does not fill the potential well, and does not produce a quasi-hydrostatic halo.

If one *does* assume that the soft component has an exponential scale height $kT/\mu m_p g$, where $g = 4\pi G\Sigma$ and Σ is the surface mass density (derived from the optical *B*-band profile under the assumption that the mass-to-light ratio is similar to that of the solar neighborhood, $\Upsilon_B = 2.3\ M_\odot\ L_\odot^{-1}$), then the peak electron density is $(2\text{–}3) \times 10^{-3}$ cm^{-3} at radii of $\sim$5 kpc. This value is 2–3 times smaller than the n_e derived for the LHB ($n_e = 0.006$ cm^{-3}, $kT = 0.108$ keV) and $\sim$5 times smaller than the densities derived from either the Eridion Bubble ($n_e \sim 0.015$ cm^{-3}, $kT = 0.17$ keV; Guo et al. 1995) or the walls of the Loop I superbubble ($n_e \sim$ 0.01–0.015 cm^{-3}; Egger 1993), but is similar to the tenuous medium filling the center of the Loop I superbubble ($n_e = 3 \times 10^{-3}$ cm^{-3}; Egger 1993). Given the softness of the LHB and its overburden (typically a few $\times\ 10^{20}$ cm^{-2}), similar objects in M101 will not contribute substantially to the *Chandra* spectrum. Assuming that the soft component is formed by a population of objects such as the Loop I Bubble or the Eridion Bubble and assuming that such objects have a significant *z*-extent, the filling fraction of hot gas would be $\sim$0.2.

If, instead, one assumes the Breitschwerdt & Schmutzler (1999) model, then the amount of truly hot gas will be a fraction of the amount indicated by the X-ray flux. Using the approximation that the flux $\propto 1/z$ given in Breitschwerdt & Schmutzler (1999), one finds that about one-third of the total flux is due to truly hot gas. Since the fraction of the total flux falling within the *Chandra* bandpass may vary with *z*-height, a better estimate must wait for detailed modeling.

The harder component has a temperature of $\sim$0.7 keV. This temperature is similar to that expected from the aggregate emission due to late-type dwarf stars ($kT \sim 0.8$ keV). We have used a model similar to that used by Kuntz & Snowden (2001) to calculate the emission by dwarfs (spectral types F through M) per square parsec in the solar neighborhood and scaled the result by the disk surface mass density. It should be noted that while the Kuntz & Snowden (2001) model was normalized to the number of K and M dwarfs in the solar neighborhood and matched the number of Galactic stellar X-ray sources at high Galactic latitude, it did not match the midplane stellar mass density. Further, the Kuntz & Snowden (2001) model, since it matched the number counts at high Galactic latitude, was not sensitive to the substantial uncertainties in the X-ray luminosities of young stars, whereas a sum through the entire disk is quite sensitive; even though there are 1/10 the number of M dwarfs in the 0.0–0.1 Gyr age range as in the 1–10 Gyr range, their X-ray luminosities are 10 times greater, so their contribution to the X-ray emission is comparable. Thus, considering the uncertainty with which one can apply the Galactic initial mass function and star formation rate to M101, the calculation of the contribution of dwarf stars to the X-ray emission in M101 is a rather uncertain estimate. We find that dwarf stars account for $\sim$35% of the 0.45–2.0 keV band flux of the harder component, only $\sim$2% of the softer component, and $\sim$10% of the total flux. The relative contributions of the unresolved stars to the hard and soft components are shown in Figure 13.

The temperature of the harder *Chandra* component is also similar to that of the "soft" Galactic component ($kT = 0.8$ keV) found by Kaneda et al. (1997) in their *ASCA* study of the Scutum arm. (Note that their soft component is much harder than the "hard" component of Kuntz & Snowden 2000.) In their case, the spectrum was modeled with a nonequilibrium model requiring $n_e t = 10^{9.1}$ cm^{-3} s. Replacing our hard MEKAL component with a nonequilibrium ionization component does little to change the fit and requires $n_e t = 10^{12.9}$ cm^{-3} s, that is, nearly an equilibrium plasma. From the fitted value of the absorbing column, Kaneda et al. (1997) estimate the effective distance to the Galactic region producing their soft emission to be $\sim$2 kpc and find a scale height of 100 pc. If their emission is produced along a 2 kpc line of sight, then the expected emission from M101 would be 1.9×10^{-7} ergs cm^2 s^{-1} sr^{-1}; the observed value for the hard component of the A+B spectrum is 4.7×10^{-8} ergs cm^2 s^{-1} sr^{-1}, only a factor of 4 smaller. If the Kaneda et al. (1997) emission is over a longer path, then the two values would be more similar. The harder component found by Kaneda et al. (1997; $kT \sim 7$ keV) is too dim to be observed by *Chandra* at the distance of M101.

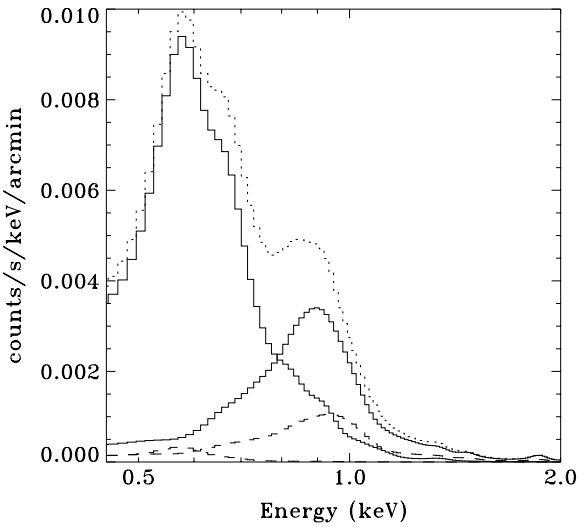

FIG. 13.—*Dotted line*: Model spectrum fit to spectrum A+B. *Solid line*: Soft and hard thermal (MEKAL) components. *Dashed line*: Contribution by dwarf stars to the soft and hard components.

Kaneda et al. (1997) attributed their 0.8 keV component to late-stage supernovae expanding into regions of low ambient density, conjecturing that supernovae are abundant, one per GIS field of view, and reheating regions previously swept by older supernovae. Although the M101 equivalent is likely to be produced by the same means as in the Milky Way, the M101 spectra do not present the evidence for nonequilibrium plasmas that would point to young SNRs. Absence of evidence is not, however, evidence of absence, and the presence of such a component may be obscured by other emission components. A further caution concerning the supernova attribution can be derived from the hydrodynamic supernova models of Shelton (1999). In those models of individual supernovae in low-density ambient media, typical time-averaged temperatures were $\lesssim 0.35$ keV, substantially cooler than the observed component. Greater ambient densities led to significantly higher emissivities, but not to significantly higher temperatures.

In M101, there are likely multiple sources for the hard component. Active star formation regions such as R136 in 30 Dor, can produce hot thermal components with $kT \sim 0.8$ keV (Wang 1999). A covering fraction of 0.1%–0.2% by 30 Dor–like objects could provide the observed emission measure for the hard component, but would overproduce the soft emission by a factor of ~ 5.

Two-component structure.—As has been mentioned above, it is not surprising that the spectrum is statistically well fitted by two components in collisional ionization equilibrium. The emission occupies only a small range of the energy interval accessible to *Chandra*, 0.45–1.0 keV, with a resolution of 0.12 keV. Within this energy interval, the emission is dominated by the O VII/O VIII lines at 0.560 and 0.650 keV and the Fe complex at 0.7–1.0 keV. The softer component produces the bulk of the oxygen flux, while the harder component produces the Fe emission. A range of temperatures probably exists, but we are determining the most common gas temperatures.

A similar problem was experienced by the even lower resolution *ROSAT* studies of the Galactic halo. Kuntz & Snowden (2000) suggested that the temperatures of the two Galactic halo components might be indicative of an isochorically cooling gas that passes through two regions of increased stability on its path down the cooling curve, an argument analogous to that made by Gehrels & Williams (1993) to explain the bimodal temperature distribution of emission from RS CVn stars.

Such an argument has a more limited applicability in this case. The cooling curve derived from the Raymond & Smith (1977) model allows regions of relative stability at $kT = 0.068$–0.121 keV [$(0.79$–$1.4) \times 10^6$ K] and $kT = 0.388$–0.646 keV [$(4.5$–$7.5) \times 10^6$ K], and similar results are obtained from the Astrophysical Plasma Emission Code (Smith et al. 2001) models (R. K. Smith 2002, private communication). Significantly altering the metallicities does change the location of the inflection points, but not significantly for the range of metallicities observed in M101. The temperature of the soft component falls several σ above the lower inflection. The temperature of the hard component is marginally incompatible with the upper limit. However, since very hot gas produced in the disk is not likely to cool isochorically and the isobaric cooling curve does not have regions of enhanced stability, the temperature of the upper component is unlikely to be due to the cooling curve.

5.2. *Bulge*

The bulge of M101, as seen in the optical data of Okamura et al. (1976), can be characterized as having an exponential profile with a scale length of 100 pc, much smaller than the bulge of the Galaxy, which has a scale length of ~ 1 kpc. In M101 the extended X-ray nucleus has a scale length similar to that of the optical bulge, and the bulge-to-disk ratio in the X-ray is similar to that of the optical. Given the small size of the bulge and the scaling of the X-ray emission with optical light, it is perhaps not surprising that, unlike the case the Galaxy, the X-ray emission in M101 does not show a marked change in temperature between disk and bulge. In the X-ray range, there are no signs of nuclear activity, and the nuclear point sources are consistent with ordinary X-ray binaries.

5.3. *Extended Halos*

Since the classic paper by Spitzer (1956), the high-energy model of galaxies has included a nearly spherical hot corona or halo, in either hydrostatic equilibrium or some similar state. The existence of such a halo seems reasonable, given that the virial temperature of a galaxy like the Milky Way is $\sim m v_c^2/2k = 2 \times 10^6$ K, where v_c is the circular velocity. Models of the soft X-ray emission from our own Galaxy usually include such a component (Wang 1998; Pietz et al. 1998), although Kuntz & Snowden (2001) suggested that the rather featureless component that dominates the *ROSAT* $\frac{3}{4}$ keV emission may, in fact, be due not to a Galactic corona but rather to cosmological sources.

Observations of other galaxies in the *ROSAT* era were generally equivocal; the only extended halos detected around nonstarburst, edge-on galaxies were arguably due to high star formation rates (NGC 4631 and NGC 891). Benson et al. (2000), noting that simple cooling flow models of galaxies predicted $L_X \propto v_c$, searched for extended X-ray halos around three massive galaxies. Although these galaxies were expected to have $L_X \sim 10^{42}$ ergs s^{-1}, the observed 95% upper limits were 3.8, 1.2, and 0.4×10^{41} ergs s^{-1}.

Toft et al. (2002), executing smoothed-particle hydrodynamic models of galaxy formation from $z \sim 20$–40 to the present, found their galaxy halos to be at least an order of magnitude fainter than the halos produced by the simple cooling flow models of galaxy formation. M101 is voluminous, but not massive. The L_X-v_c relation found by Toft et al. (2002) suggests that M101 ($v_c \sim 170$ km s^{-1}) should have a halo with $L_X = (1$–$3) \times 10^{38}$ ergs s^{-1} in the 0.2–2.0 keV band, $T \leq 10^6$ K, and the X-ray emission fairly closely confined to the disk.

Figure 14 shows the radial profile of M101 between position angles 60° and 110° (measured from north). At radii greater than ~ 7 kpc, the observed flux drops sharply to the value of the background measured by *ROSAT*; the 2 σ upper limit is 9×10^{-16} ergs cm^{-2} s^{-1} in 0.45–1.0 keV. Thus, any axisymmetric halo must make an insignificant contribution beyond this radius.

The Toft et al. (2002) value for halo luminosity is 7%–20% of the measured 0.2–2.0 keV luminosity of the diffuse emission within 7′. Whether this observation allows a halo of this magnitude is difficult to determine, the determination being sensitive to the assumed form of the correlation between the X-ray emission and the tracers of star formation (FUV, Hα, optical, etc.). Since the X-ray emission, like the optical emission, drops precipitously for the interarm

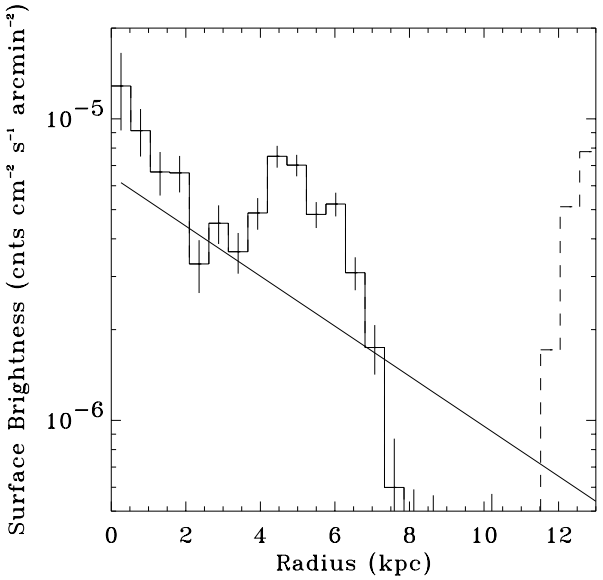

FIG. 14.—Radial profile for position angles 60°–110°. The solid line excludes the giant H II regions; the dashed line includes the giant H II regions.

region (see Fig. 14), an X-ray halo due to a dark matter potential must have a small scale length. If one assumes the profile of the X-ray halo to be

$$\rho(r) = \rho_0 \left[1 + \left(\frac{r}{r_c}\right)^2\right]^{-3\beta/2}, \quad (1)$$

where $\beta \lesssim \frac{2}{3}$, the true strength of an X-ray halo not due to disk processes is likely to be much smaller than the 7%–20% predicted by Toft et al. (2002). If one assumes a halo profile with $\beta = 1$, a halo strength comparable to or greater than the Toft et al. (2002) value is not unreasonable.

5.4. *Flotsam*

Nucleosynthetic studies of the Milky Way suggest that galaxies continue to accrete material, $\sim 1\ M_\odot\ \mathrm{yr}^{-1}$ for the Galaxy (Alibés et al. 2001; Timmes et al. 1995), and generally cite the (as yet unknown) mass of high-velocity clouds as a plausibility argument. The luminosity due to the infalling material should be $\sim 10^{40}$ ergs s^{-1}, 5 times the observed amount of diffuse X-ray emission in this *Chandra* observation. This point may not be consequential since estimates for the current infall rate required for nucleosynthesis appear to have at least a factor of 3 uncertainty (e.g., compare Alibés et al. 2001 with Timmes et al. 1995). Further, given the structure of high-velocity clouds, the infall is likely episodic. However, M101 appears to be abundant in high-velocity gas, having $\sim 2 \times 10^8\ M_\odot$ (Kamphuis 1993). Unfortunately, this gas is situated entirely outside of the field of view of this *Chandra* observation; *XMM-Newton* may be able to determine to what low level the high-velocity cloud/halo interface shock contributes to the diffuse X-ray emission.

6. SUMMARY

The bulk of the truly diffuse emission from M101 traces the spiral arms and is correlated with Hα and FUV emission, implying that it is due to ongoing star formation: hot winds from massive young stars, supernovae, and superbubbles. The spectrum of the diffuse disk emission is characterized by two thermal components with temperatures $kT = 0.20$ and 0.75 keV. The ratio of the emission measures is roughly constant across the face of the galaxy, with $\mathrm{EM_{soft}}/\mathrm{EM_{hard}} \sim 3$. Comparison of the temperatures and emission measures of these components to diffuse features in the Galaxy or the Magellanic Clouds suggests that a significant fraction of the gas forming the soft component is extraplanar. The hard component in M101 is similar to the soft Galactic ridge component seen in the Milky Way, but contains a substantial contribution from dwarf stars.

We do not find evidence for an axisymmetric halo tracing the dark matter potential. At a radius of $\sim$7 kpc, the deep interarm region shows no sign of X-ray emission above the level of the background. Given that M101 is a fairly low mass galaxy, the lack of such a halo may not be surprising.

Whether M101 has a true nuclear source remains unknown. The diffuse emission from the highest surface brightness portion of the nucleus has a spectrum consistent with thermal bremsstrahlung absorbed by about half of the total M101 column density in that direction. The remainder of the nuclear emission has a spectrum consistent with that of the diffuse disk emission.

The giant H II regions NGC 5461 and NGC 5462 are composed of truly diffuse emission whose spectral shape is similar to that of the disk emission, but the total number of counts is too small to allow detailed spectral fitting. The nonthermal component in these spectra appears to be small.

This research was supported in part by *Chandra* GO grant 01900441. The CO moment map was very kindly provided by T. Helfer. J. Kamphuis provided the H I map. The optical image was extracted from the Digital Sky Survey; the original image was obtained using the Oschin Schmidt Telescope on Palomar Mountain. The Palomar Observatory Sky Survey was funded by the National Geographic Society. The Oschin Schmidt Telescope is operated by the California Institue of Technology and Palomar Observatory. The plates were processed into the present compressed digital format with their permission. The Digitized Sky Survey was produced at the Space Telescope Science Institute (STScI) under US Government grant NAG W-2166. We would like to thank R. Mushotzky and K. Arnaud for many interesting conversations about the data and their meanings. We would like to thank the many at CXC who aided our understanding of the ACIS background. Finally, we would like to thank S. Points, the referee, for concise and insightful comments.

REFERENCES

Alibés, A., Labay, J., & Canal, R. 2001, A&A, 370, 1103
Beck, R., & Golla, G. 1988, A&A, 191, L9
Benson, A. J., Bower, R. G., Frenk, C. S., & White, S. D. M. 2000, MNRAS, 314, 557
Binney, J., & Merrifield, M. 1998, Galactic Astronomy (Princeton: Princeton Univ. Press)
Bottema, R. 1993, A&A, 275, 16
Breitschwerdt, D., & Schmutzler, T. 1999, A&A, 347, 650
Cen, R., & Ostriker, J. P. 1999, ApJ, 514, 1
Chen, L.-W., Fabian, A. C., & Gendreau, K. C. 1997, MNRAS, 285, 449
Comte, G., Monnet, G., & Rosado, M. 1979, A&A, 72, 73

Dame, T. M. 1993, in AIP Conf. Proc. 278, Back to the Galaxy, ed. S. S. Holt & F. Verter (New York: AIP), 267
de Avillez, M. A. 2000, MNRAS, 315, 479
Egger, R. 1993, Ph.D. thesis, Technische Univ. Munich
Egger, R., & Aschenbach, B. 1995, A&A, 294, L25
Evans, I. N. 1986, ApJ, 309, 544
Fraternali, F., Cappi, M., Sancisi, R., & Osterloo, T. 2002, ApJ, 578, 109
Fullmer, L., & Lonsdale, C. J. 1989, Catalogued Galaxies and Quasars observed in the *IRAS* Survey, Version 2 (Pasadena: Jet Propulsion Laboratory)
Garnett, D. R. 1989, ApJ, 345, 282
Garnett, D. R., & Kennicut, R. C., Jr. 1994, ApJ, 426, 123
Garnett, D. R., Shields, G. A., Peimbert, M., Torres-Peimbert, S., Skillman, E. D., Dufour, R. J., Terlevitch, E., & Terlevitch, R. J. 1999, ApJ, 513, 168
Gehrels, N., & Williams, E. D. 1993, ApJ, 418, L25
Grimm, H.-J., Gilfanov, M., & Sunyaev, R. 2002, A&A, 391, 923
Guo, Z., Burrows, D. N., Sanders, W. T., Snowden, S. L., & Penprase, B. E. 1995, ApJ, 453, 256
Hartmann, D., & Burton, W. B. 1997, Atlas of Galactic Neutral Hydrogen (Cambridge: Cambridge Univ. Press)
Helfer, T. T., Thornly, M. D., Regan, M. W., Wong, T., Sheth, K., Vogel, S. N., Blitz, L., & Bock, D. C.-J. 2003, ApJS, 145, 259
Hodge, P. W., Gurwell, M., Goldader, J. D., & Kennicutt, R. C., Jr. 1990, ApJS, 73, 661
Irwin, J. A., Sarazin, C. L., & Bregman, J. N. 2002, ApJ, 570, 152
Israel, F. P., Goss, W. M., & Allen, R. J. 1975, A&A, 40, 421
Kahn, F. D. 1991, in IAU Symp. 144, The Interstellar Disk-Halo Connection in Galaxies, ed. H. Bloemen (Dordrecht: Kluwer), 1
———. 1998, in IAU Colloq. 166, The Local Bubble and Beyond, ed. D. Breitschwerdt, M. Freyberg, & J. Trümper (Berlin: Springer), 483
Kamphuis, J. 1993, Ph.D. thesis, Rijksuniversiteit Groningen
Kaneda, H., Makishima, K., Yamauchi, S., Koyama, K., Matsuzaki, K., & Yamasaki, N. Y. 1997, ApJ, 491, 638
Kenney, J. D. P., Scoville, N. Z., & Wilson, C. D. 1991, ApJ, 366, 432
Kenney, J. D. P., Wilson, C. D., Scoville, N. Z., Devereux, N. A., & Young, J. S. 1992, ApJ, 395, L79
Kerr, F. J. 1993, in AIP Conf. Proc. 278, Back to the Galaxy, ed. S. S. Holt & F. Verter (New York: AIP), 3
Kregel, M., van der Kruit, P. C., & de Grijs, R. 2002, MNRAS, 334, 646
Kuntz, K. D., & Snowden, S. L. 2000, ApJ, 543, 195
———. 2001, ApJ, 554, 684
Liedahl, D. A., Osterheld, A. L., & Goldstein, W. H. 1995, ApJ, 438, L115
Little, B., & Tremaine, S. 1987, ApJ, 320, 493
Lockman, F. J., & Gehman, C. S. 1991, ApJ, 382, 182
Matonick, D. M., & Fesen, R. A. 1997, ApJS, 112, 49
McCammon, D., & Sanders, W. T. 1984, ApJ, 287, 167
Mewe, R., Gronenschild, E., & van den Oord, G. H. J. 1985, A&AS, 62, 197
Mewe, R., Lemen, J. R., & van den Oord, G. H. J. 1986, A&AS, 65, 511
Moody, J. W., Roming, P. W. A., Joner, M. D., Hintz, E. G., Geisler, D., Durrell, P. R., Scoween, P. A., & Jee, R. O. 1995, AJ, 110, 2088
Mukai, K., Pence, W. D., Snowden, S. L., & Kuntz, K. D. 2003, ApJ, 582, 184
Mushotzky, R. F., Cowie, L. L., Barger, A. J., & Arnaud, K. A. 2000, Nature, 404, 459
Okamura, S., Kanazawa, T., & Kodaira, K. 1976, PASJ, 28, 329
Pence, W. D., Snowden, S. L., Mukai, K., & Kuntz, K. D. 2001, ApJ, 561, 189
Pietz, J., Kerp, J., Kalberla, P., Burton, W. B., Hartmann, D., & Mebold, U. 1998, A&A, 332, 55
Rand, R. J. 1998, Publ. Astron. Soc. Australia, 15, 106
Raymond, J. C., & Smith, B. W. 1977, ApJS, 35, 419
Shelton, R. L. 1999, ApJ, 521, 217
Smith, R. K., Brickhouse, N. S., Liedahl, D. A., & Raymond, J. C. 2001, ApJ, 556, L91
Snowden, S. L. 2001, in The Century of Space Science, ed. J. Bleeker, J. Geiss, & M. Huber (Dordrecht: Kluwer), 581
Snowden, S. L., Egger, R., Finkbeiner, D., Freyberg, M. J., & Plucinsky, P. P. 1998, ApJ, 493, 715
Snowden, S. L., Freyberg, M. J., Kuntz, K. D., & Sanders, W. T. 2000, ApJS, 128, 171
Snowden, S. L., Mukai, K., Pence, W., & Kuntz, K. D. 2001, AJ, 121, 3001
Snowden, S. L., & Pietsch, W. 1995, ApJ, 452, 627
Snowden, S. L., et al. 1997, ApJ, 485, 125
Sodroski, T. J., Odegard, N., Arendt, R. G., Dwek, E., Weiland, J. L., Hauser, M. G., & Kelsall, T. 1997, ApJ, 480, 173
Spitzer, L. 1956, ApJ, 124, 20
Stecher, T. P., et al. 1997, PASP, 109, 584
Stetson, P. B., et al. 1998, ApJ, 508, 491
Timmes, F. X., Woosley, S. E., & Weaver, T. A. 1995, ApJS, 98, 617
Toft, S., Rasmussen, J., Sommer-Larsen, J., & Pedersen, K. 2002, MNRAS, 335, 799
Torres-Peimbert, S., Peimbert, M., & Fierro, J. 1989, ApJ, 345, 186
Trinchieri, G., Fabbiano, G., & Romaine, S. 1990, ApJ, 356, 110
Tully, R. B. 1988, Nearby Galaxies Catalogue (Cambridge: Cambridge Univ. Press)
van der Kruit, P. C. 1988, A&A, 192, 117
———. 1990, in The Milky Way as a Galaxy, ed. R. Buser & I. King (Mill Valley: Univ. Science Books), 77
van der Kruit, P. C., & Searle, L. 1982, A&A, 110, 79
Wang, Q. D. 1998, in IAU Colloq. 166, The Local Bubble and Beyond, ed. D. Breitschwerdt, M. Freyberg, & J. Trümper (Berlin: Springer), 503
———. 1999, ApJ, 510, L139
Wang, Q. D., Immler, S., & Pietsch, W. 1999, ApJ, 523, 121
Williams, R. M., & Chu, Y.-H. 1995, ApJ, 439, 132
Zaritsky, D., Elston, R., & Hill, J. M. 1990, AJ, 99, 1108